Chapter 4

Electron Spin Resonance Study of As-grown and High Energy Electron Irradiation-Induced Hexagonal GaN Layer on Sapphire Substrate

4.1 Introduction

The role of defects in semiconductors in doping, compensation, phase stability and device performances as well as the kinetics of formation defects during the growth of materials under non-equilibrium conditions were not well investigated.

As-grown GaN films on sapphire are generally n-type [1, 2, 3] with carrier concentrations between 10^{16} and 10^{19} cm^{-3}, although insulating and p-type GaN films have been reported. The residual donor has not been positively identified and N vacancy [4], residual oxygen substitutionally incorporated on to N sites [5] and interface defects [6] have been postulated to be the dominant donor species. These proposed donor identifications were based on the growth kinetics and chemical analysis of lower quality material which had been grown before higher quality of source gases in an epitaxial growth and advanced growth techniques became common place. It is not clear how applicable those arguments are to current carrier concentrations of 10^{16} - 10^{17} cm^{-3}.

Although high-energy electron irradiation has been used extensively in the past to study vacancy defects in Si [7], GaAs [8] and ZnSe [9], only three recent studies have been conducted in GaN [10, 11, 12]. Linda *et al.* [10] used an optically detected magnetic resonance (ODMR) of a photoluminescence band at 0.93 eV, produced by 2 MeV electron irradiation, to obtain a tentative identification of a Ga-interstitial complex on the basis of ODMR hyperfine interaction. Look *et al.* [11] used temperature dependent Hall measurements to identify N-vacancy/N-interstitial Frenkel pairs produced by produced by 0.7 - 1 MeV electron irradiation. According to them, the N vacancy was shown to have a donor level at 0.07 eV below the bottom of conduction band. Fang *et al.* [12] used a deep level transient spectroscopy (DLTS) to reveal an 1 MeV electron irradiation-induced electron trap level at 0.18 eV below the bottom of conduction band. This trap is mostly like associated with an N vacancy.

In this chapter, the electron spin resonance (ESR) studies of as-grown and electron irradiated n-type hexagonal GaN films on sapphire will be discussed. To the best of my knowledge, the detailed discussion of the influence of high energy electron irradiation on the yellow and UV

luminescence transitions in n-GaN has not reported yet.

4.2 Difficulties in ESR Measurements

In case of GaN film on sapphire substrate, there are lots of ESR signals arising from sapphire substrate (back ground signals) due to transition metal ion impurities (Fe, V etc.). These signals have to be separated whether they are arising from the sapphire substrate or GaN epitaxial layer. Background signals were found to have the following ESR characteristics in comparison with signals from a GaN film.

1. Background signals, in fact, move very fast when changing the orientation of c-axis of sapphire substrate with respect to the magnetic field.

2. ESR intensities of background signals are easily saturated at low microwave powers around 1 mW.

Thus, the GaN-related ESR lines are easily separated by carefully aligning the samples and by saturating the background signals with increasing the microwave power.

4.3 Experimental

4.3.1 Sample preparation

The GaN materials used in this study was grown in a metal organic chemical vapor deposition (MOCVD) reactor operating at a atmospheric pressure. A 30-nm-thick GaN buffer layer deposited on (0001)-oriented sapphire substrate at 530°C. Over the low-temperature GaN buffer a 2.4-μm-thick Si (n-type dopant) doped GaN film with different carrier concentrations were grown at 1050°C. Van der Pauw Hall measurements of carrier concentration and mobility were performed on each samples at 300 K. The samples with carrier concentrations between 1.3×10^{16} - 8.4×10^{18} cm^{-3} were used in this study.

4.3.2 ESR system setup

ESR measurements were performed in a Bruker 300ESP X-band (9.5 GHz) spectrometer equipped withe an Oxford liquid-helium flow cryostat for temperature control from 3.1 K to 300 K at Okazaki National Research Institute. Some of samples were measured in a JEOL JES-FE1XG X-band (9.5 GHz) spectrometer equipped with liquid-helium (4.2 K) at Nagoya Institute of Technology. A 100 kHz modulation of the microwave intensity and a TE_{011} cylindrical cavity which had a grid for the illumination of the sample were used in both ESR systems. The maximum power incident into the cavity was 200 mW. An α, α'-diphenyl-β-picrylhydrazyl reference was used to evaluate the g value of different paramagnetic centers.

4.4 ESR Properties in As-grown GaN

In this section, the analysis of ESR spectra obtained from as-grown n-type GaN samples will be discussed.

4.4.1 ESR resonance and fundamental properties

A narrow portion of the ESR spectra for a carrier concentration of 1.5×10^{17} cm^{-3} at 300 K is shown in Fig. 4.1(a). The position of the ESR resonance is $B_0 = h\nu/g\beta - B_n$, where ν is the resonance frequency, β is the Bohr magneton, g is the Landé g value and B_n is due to the effect of residual hyperfine interaction. A sharp Lorentzian resonance line is observed at $g = 1.9541$ and

the peak-to-peak linewidth (Δ_{pp}) is about 10.5 G at 4.2 K in all samples with different carrier concentrations. The values of g and ΔH_{pp} are very close to those reported by AsifKhan *et al.* [13]. However, the clear ESR spectra was not observed for samples with carrier concentration above 5×10^{17} cm^{-3}. There is a slight anisotropy with the c direction as the principle axis shown in Fig. 4.1(b), and $g_{\parallel} = 1.9545$ and $g_{\perp} = 1.9451$. The orientation dependence of the g value is fitted by $\left(g_{\parallel}^2 \cos^2\theta + g_{\perp}^2 \sin^2\theta\right)^{1/2}$, where θ is the angle between the c axis and the magnetic field. The degree of $(g_{\parallel} - g_{\perp})$ and the average g value are similar to those observed for donor in ZnO [14] whose band structure is similar to that of GaN. It should be noted that the Lorentzian spectra is the ESR line which comes from the GaN film (not from the sapphire substrate).

The g value is near 2, as expected for donor or conduction electrons in wide bandgap semiconductors and a slight anisotropy is consistent with the GaN hexagonal symmetry. The observed ESR resonance is much narrower than that for isolated centers in other III–V semiconductors whose resonance are broadened by residual hyperfine interaction with the lattice nuclei [15]. Moreover, in all samples in this study, the linewidth of resonance narrows with increasing temperature up to T_{min}, which is the temperature at the narrowest linewidth, due to exchange or motional averaging of the residual hyperfine broadening effect. For a case of conduction band ESR, a linewidth would not show this phenomena. However, this line width broadening is often seen as resonance due to impurity donor band where the averaging interaction (exchange narrowing) increases with increasing temperature. The signal is not easily saturated by microwave power up to 50 mW and this result indicates that the resonance is due to a delocalized center rather than a localized center.

At this time, based on g value and temperature and microwave power dependencies of ESR linewidth, the observed ESR resonance from n-GaN is attributed to

1. electrons in the conduction band or shallow donor level (g value characteristic),
2. donor band rather than isolated donors or electron in the conduction band (linewidth characteristic).

4.4.2 Five-band k·p model and conduction band g value

In Fig. 4.2(a), the energy dispersion for GaN at the Γ point valence band maximum (VBM) without the spin-orbit interaction is shown. The spin-orbit interaction and the noncubic crystal-field split the VBM into three states, Γ_9^v, $\Gamma_7^{v(1)}$ and $\Gamma_7^{v(2)}$, which would be a doubly degenerate Γ_6^v state and a singly degenerate Γ_1^v state in absence of spin-orbit interaction.

The g value of the conduction electron g_e and effective mass m^* was analyzed by using five-band **k**·**p** model, defined schematically in Fig. 4.2(b), calculation. According to this model, the g_e value is given by

$$\frac{g^*}{g_e} - 1 = -\frac{P^2}{3}\left[\frac{\Delta_0}{E_0(E_0+\Delta_0)} + \lambda^2 \frac{\Delta_0'}{(E_0' - E_0)(E_0' - E_0 - \Delta_0')}\right], \tag{4.1}$$

where g_e is the free electron g value which is 2.0023. In the wide bandgap semiconductors such as GaN the spin-orbit interactions are smaller than the energy gap. For many direct bandgap semiconductors, the first term in the equation for g_c (due to the interaction with the valence band) is dominated. However, this is not the case for GaN. The spin-orbit interaction of the valence band is due to the N (anion) and is 0.0011 eV for GaN [16], while higher conduction band is due to gallium (cation) that might be comparable to that of GaAs (0.2 eV) [17]. The m^* in five-band **k**·**p** model is given by

$$\frac{m_0}{m^*} - 1 = \frac{P^2}{3}\left[\frac{3E_0 + 2\Delta_0}{E_0(E_0+\Delta_0)} - \lambda^2 \frac{3(E_0' - E_0) - 2\Delta_0'}{(E_0' - E_0)(E_0' - E_0 - \Delta_0')}\right], \tag{4.2}$$

where m_0 is the free electron mass. This takes into account the interaction of the Γ_1 conduction band with the spin-orbit split Γ_6 valence band and conduction bands.

The matrix elements coupling between the Γ_1 conduction band and Γ_6 conduction band ($\lambda^2 P^2$), and the Γ_1 conduction band and valence band (P^2) are given by

$$\lambda^2 P^2 = \frac{2}{m_0} \left|\langle \Gamma_{1c} \left| p_x \right| \Gamma_{6c,x} \rangle\right|^2, \tag{4.3}$$

$$P^2 = \frac{2}{m_0} \left|\langle \Gamma_{1c} \left| p_x \right| \Gamma_{6v,x} \rangle\right|^2. \tag{4.4}$$

In the parameters in eqs. (4.1) and (4.2), some are well established, some have experimental values with uncertainties. These two equations have a total eight parameters (g_c, Δ_0, E_0, $E_0^{'}$, m^*, P^2, λ^2 $\Delta_0^{'}$). The conduction band effective mass is calculated $0.2 \cdot m_0 \pm 10\%$ by the infrared absorption due to free carriers [18, 19]. The valence band spin-orbit interaction Δ_{so} is measured to be 11 meV [16] and $E_0^{'}$ is measured to be 8.5 ± 0.2 eV from UV reflectivity measurements [20] and the art first-principles total-energy calculations. Thus, three of eight parameters (P^2, λ^2 $\Delta_0^{'}$) are still unknow. Using eqs. (4.1) and (4.2) with measured g_c in this study, two of three unknow parameters can be related each other as shown in Fig. 4.3. In other III–V semiconductors, P^2 is in the range between 15 and 30 eV using the accurate g_c and m^* [21] or somewhat lower in the more ionic semiconductors. Thus, P^2 is set to $10 < P^2 < 30$. For λ^2, it is estimated to be in the range $0.3 < \lambda^2 < 0.6$ based in covalent semiconductor such as GaAs [22]. The spin-orbit interaction of Γ_6 conduction band is primarily determined by Ga cation and $\Delta_0^{'}$ is estimated in the range $0.1 < \Delta_0^{'} < 0.3$ eV based on Ga compound semiconductors. Considering above estimation, the values of three parameters (P^2, λ^2 $\Delta_0^{'}$) are reduced to the range $16.7 < P^2 < 22.5$ eV, $0.3 < \lambda^2 < 0.6$ and $0.1 < \Delta_0^{'} < 0.3$ eV. It should be noted that the only averaged g_c is used since the experimental anisotropy of the effective-mass has not been reported yet.

4.4.3 ESR resonance intensity and linewidth

Figure 4.4(a) shows the temperature dependence of the ESR intensity (normalized to the ESR intensity obtained 3 K), which does not follow the Curier-Weiss law clearly. This result suggests that the observed resonance are not localized in deep centers. Additional arguments to conclusion are lack of the nuclear hyperfine structure or superhyperfine structure, expected for localized electrons in intrinsic defects of III–V semiconductors. The lack of hyperfine structure would be due to Overhauser effect which has been observed in III–V semiconductor [23, 24]. Recently, Denninger *et al.* have determined the Overhauser shift, the paramagnetic shift (Knight shift) and the Dynamic Nuclear Polarization resulting from the coupling of the shallow donor in GaN is due to the nuclei of the lattice by ESR-NMR method [25].

Figure 4.4(b) (plotted as a function of inverse temperature to emphasize the low-temperature regime) and Fig. 4.5 (plotted as a function of temperature) show the temperature dependence of the ESR linewidth. The resonance at temperature higher than 50 K was not observed due to broadening of the line with increasing temperature. The minimum in the linewidth is observed temperature (T_{min}) at 25 K. In general, this T_{min} is occurred due to the competition between narrowing due to averaging of the residual hyperfine structures at below T_{min} and broadening due to electron-phonon interaction at higher T_{min}.

An decrease in linewidth with increasing temperature ($T \leq T_{min}$) has been reported for donors in other III–V semiconductors such as O vacancy in ZnO [26] and residual donors in InSb [27]. These effects are attributed to an averaging of nuclear hyperfine interactions either through exchange interactions or motion of the electrons from one site to another in an impurity band (hopping conduction) [22, 29]. An increase in exchange narrowing of the donor resonance with increasing temperature is attributed to an increase in the conduction electron concentration and an increase in the interaction of the donor electrons with those electrons or to an increase in the interaction between donor electrons as those become delocalized [28]. In this study, the narrowing is observed at at low temperature ($T < 25$ K) where the concentration of conduction electrons is almost constant but donor electrons are already interacting. Thus, ESR linewidth narrowing is believed to be due to motional effects or hopping mechanism.

The electrical conductivity (σ) of one of the investigated films measured by van der Pauw Hall measurement is shown in Fig. 4.6 as a function of inverse temperature. The data fit the expression

$$\sigma = \sigma_1 \exp(-\varepsilon_1/kT) + \sigma_2 \exp(-\varepsilon_2/kT), \tag{4.5}$$

where the activation energies ε_1 and ε_2 are 19.2 and 0.68 meV, respectively. The conductivity data indicates a hopping conduction below $\sim$ 30 K with an activation energy $\varepsilon_2 = 0.68$ meV due to overlap of the shallow donor wave functions and presence of compensating defects [30]. In the case of hopping motion of electrons, the linewidth is inversely proportional to the probability p of the phonon-assisted transition from one center to another, $\Delta H_{pp} \propto 1/p$. This probability depends on temperature [30, 31] and is given by

$$p \propto \left[\exp\left(\frac{\varepsilon_2}{kT}\right) - 1\right]^{-1}. \tag{4.6}$$

The expectation of eq. (4.6), as shown in Fig. 4.5 (solid line), agrees to the data below 25 K, where the linewidth decreases with increasing temperature.

At higher temperatures regime ($T \geq T_{min}$), the linewidth increase with increasing temperature due to the interaction of electrons with acoustic phonons. In semiconductor, the inverse of the linewidth of delocalized electrons is approximately equal to the spin-lattice relaxation time (T_1), which is related to the temperature and electron-phonon interaction, and is given by

$$\frac{1}{T_1} \propto \frac{T}{\mu_L}, \tag{4.7}$$

where μ_L is the electron mobility due to the electron-phonon interaction. In these low-temperature regime, it is good approximation to limit μ_L to the interaction with acoustic phonons. Thus, the electron mobility is proportional to $T^{-3/2}$ and the linewidth is proportional to $T^{5/2}$ from eq. (4.7). The dashed line in Fig. 4.5 shows the result fitted by $T^{5/2}$ and is good agreement with the data above 25 K.

4.5 Optical and ESR Properties in Electron Irradiation-Induced n-GaN

In this section, the yellow luminescence band in high energy 7 MeV electron irradiated n-GaN was investigated as a function of electron irradiation dose. The change of the luminescence intensity ratio between yellow band and near-band-edge (yellow-to-UV luminescence intensity ratio) with changing the electron irradiation dose generated by high energy electron accelerator characterized by photoluminescence measurements and low-temperature ESR techniques will be discussed. A theoretical model developed for the yellow-to-near-band-edge intensity ratio based on rate equations will be also discussed.

4.5.1 Sample and high energy electron irradiation

The samples chosen in this study were four pieces of GaN samples, which were cut from a 4-μm-thick n-type GaN on sapphire substrate, with carrier concentration 1.7×10^{17} cm^{-3}.

Samples were enveloped by an Al foil and irradiated with with doses (F) of 1×10^{15} , 1×10^{16} and 1×10^{17} electrons/cm^2 at 7 MeV electrons from an electron linear accelerator (LINIAC) at Osaka Prefecture University with pulse width 4 μsec, a density duty ratio 30 Hz and a total electro-beam current of 10μA/cm^2. During irradiation, temperature of samples were held close to 300 K by water cooling of the sample holder.

The expected range for 7 MeV electrons in GaN is over 330 μm, from the Katz-Penhold relationship [32, 33]; thus, energy loss may be neglected in a 4 μm-thick GaN. The irradiation with 7 MeV electrons is expected to produce N and/or Ga vacancies in GaN.

4.5.2 Photoluminescence properties and theoretical model

The room-temperature photoluminescence measurements were performed using He–Cd laser emitting at 325 nm. The luminescence was disperse in a 1 m spectrometer, detected by a photomultiplier using "lock-in" technique.

The room-temperature photoluminescence spectra of as-grown and irradiated samples are shown in Fig. 4.7(a), where the luminescence intensity is normalized to the emission around 3.4 eV (*ultraviolet* : UV) intensity. The spectra display two distinct features namely the near-band-edge transition at 3.4 eV UV luminescence and the broad band emission centered around 2.2 eV (*yellow*). The yellow band exhibits a periodic intensity modulation due to microcavity effects [34]. Inspection of Figs. 4.7(a) and 4.7(b) reveal that the yellow luminescence drastically increases with the electron fluence. Furthermore, the integrated intensity of the yellow luminescence band also increases as irradiation dose is increased. It should be noted that absolute luminescence intensities associated with the UV and yellow decrease with increasing the electron irradiation dose.

Although photoluminescence reveals a distinct optical signature of defect such as the yellow luminescence, the microstructure and chemical nature of defect has not been identified yet. Ogino and Aoki [35] proposed that the yellow luminescence comes from a shallow donor and a deep acceptor which can be described by configuration coordinate model. Neugebauer and Van de Walle [36] proposed that the native Ga vacancy is origin of the yellow luminescence using the first-principle calculation. Other models [37] propose that the yellow luminescence is due to C acceptors, double donors and intrinsic defects related to dislocations.

To make a interpretation of the yellow-to-UV intensity ratio as shown in Fig. 4.7, a theoretical model was developed. The model takes into account the dominant optical transition in GaN, that is, UV and yellow transitions. The yellow transition involves a Shocley-Read type transition with single deep level in the bandgap. The as-grown GaN in this study has an n-type conductivity with $n = N_D$. The free electron and hole concentrations are $n \approx N$ and $p \gg p_0$, respectively under low-density excitation. Assuming that the charge state of the deep level is either neutral or negative, the total deep level concentration is given by $N_T = N_T^0 + N_T^-$, where N_T^0 and N_T^- are the concentrations of neutral and negatively charged (ionized) deep levels, respectively. The free electron and hole concentrations are $n \approx N_D - N_T^-$ and $p \gg p_0$, respectively under low-density excitation.

The rate equations for the UV and yellow transitions will be derived. These equations enable one to deduce the dependence of the deep level concentration on the electron electron irradiation dose by comparing between theoretical and experimental results.

The intensity of the UV transition is expressed by

$$I_{UV} = B \cdot n \cdot p = B \cdot N_D \cdot p, \tag{4.8}$$

where B is the bimolecular recombination coefficient. The deep level transition consists of two transitions, that is, the conduction-band-to-deep-level transition with rate $_1$ and the deep-level-to-valence-band transition with rate I_2, which are given by

$$I_1 = C_1 \cdot n \cdot N_T^0 = C_1 \cdot N_D \cdot N_T^0, \tag{4.9}$$

and

$$I_2 = C_2 \cdot N_T^- \cdot p, \tag{4.10}$$

where C_1 and C_2 are constants. Equations (4.9) and (4.10) are occurred sequentially and thus, $I_1 = I_2$ under steady-state conditions. In the case of $n \gg p$, this condition leads to the inequality as $N_T^- \gg N_T^0$. Thus, most of the deep centers are occupied at low excitation

$$N_T = N_T^0 + N_T^- \approx N_T^-. \tag{4.11}$$

The rate of the UV and yellow luminescence intensity ratio can be obtained by dividing eq. (4.8) by eq. (4.10). Assuming $I_2 = I_{yellow}$, the intensity ratio is given by

$$ratio(= I_{Yellow}/I_{UV}) = \frac{C_2 \cdot N_T \cdot p}{B \cdot (N_D - N_T) \cdot p} \tag{4.12}$$

$$
\begin{aligned}
&\simeq \frac{C_2 \cdot N_{T0}}{B \cdot (N_D - N_{T0})}\left(1 + \frac{N_D \cdot \alpha}{N_d \cdot (N_D - N_{T0})} \cdot F\right) \\
&\propto 1 + \beta \cdot F.
\end{aligned}
$$

Here we assume $N_T = N_{T0} + \alpha F$ where N_{T0} is the initial deep level concentration, α and β are the constants. The final simple equation in eq. (4.12) shows that the yellow-to-UV ratio is proportional to electron irradiation dose F if the deep level concentration independent of the doping concentration. The high energy electron irradiation introduced several defects such as vacancy and these form several deep-lying defect levels in the bandgap of semiconductors, which are induced at different production rate. Whether these defects act as acceptors or donors depends on the limiting position of the Fermi level. Thus, N_T depends on the electron irradiation dose. In the proposed model, the high energy electron irradiation introduces the defect which forms a compensating deep acceptor level in n-type GaN.

4.5.3 ESR and LESR properties

Figure 4.8 shows ESR spectra measured at 4.2 K. The sharp Lorentzian resonance line due to the conduction electron discussed in § 4.4.1 and § 4.4.2 are observed. No other specific signal was observed. The ESR signal intensity decreases as increase in the electron irradiation dose. This is due to the conduction electron concentration. Since the resistivity shown in Fig. 4.9 increases with increasing the electron irradiation dose due to the trapping of electrons at defects levels, as well as lowering of Fermi level.

ESR provides detailed information on the microscopic structure of paramagnetic states in semiconductor. In GaN, several groups have studied the ESR signature of residual donor at low temperature [28, 13]. However, due to low sensitivity of this method, thick samples have to be studied.

To detect other resonance from the electron irradiated samples in ESR, the defect state has to be paramagnetic, i.e. the Fermi level must be at about the same position as the defect. However, due to the native background doping the Fermi level is generally near the conduction band and the deep defect therefore doubly occupied and not accessible to the standard ESR. The Fermi level of the electron irradiated samples are still near conduction band even in highest electron irradiation dose (1×10^{17} cm^{-2}). This can be overcome be illuminating the sample which leads to the excitation of electrons from the deep defects states and provides singly-occupied, paramagnetic defects. This technique is called light-induced electron spin resonance (LESR). LESR can not only provide information about defect specific quantities such as number of spins but furthermore about energetic levels of diamagnetic to paramagnetic transition of centers located in the bandgap and about excitation dynamics.

The LESR was excited with the light of a 300 W Xe lamp and introduced into the cavity by a glass fiber. The problem with a lamp is that the coupling into the cavity by a optical fiber reduces the initial light power to roughly $\approx 50\%$. In general, a light power is very essential. The more the better. The LESR and ESR spectra are shown in Figs. 4.10(a) and 4.10(b) with the sample c-axis oriented perpendicular to the external magnetic filed.

The numerical difference between the illuminated and dark conditions reveals centers transition from diamagnetic to paramagnetic. This transitions (processes) at extremely low-temperature are all very very slow. Because of limiting the low-temperature facility, the samples were excited from 3 to 10 hours in this study. The resonance just grew slowly almost linearly with a 20-30 sec fast component. And only after several hours of illumination saturation of the slow component was observed. However, no other specific resonance was observed in LESR studies except resonance due to the conduction electron. The change in the intensity of the resonance due to the conduction electron depends much on electron irradiation dose. The intensity change of the sample with an electron irradiation dose of 1×10^{17} cm^{-2} is larger than that of 1×10^{16} cm^{-2}. There is no difference in the ESR linewidth (peak-to-peak) and the shape of line between dark and illuminated conditions. The defect production rates ($\tau = \Delta N/\Delta F$) are obtained from

spin densities of difference spectra (illumination - dark) as $\tau = 1.2 - 1.6$ cm^{-1} for all electron irradiated samples.

When switching off the light source, the signal relaxes back to its initial value with a rate faster than the experimental resolution of 5 s.

4.5.4 Deep defect model

The failure in observation of deep defect states from electron irradiated n-GaN samples by ESR or LESR prevents from one to investigate a detail defect model regarding to yellow luminescence. Now the important results deduced from this study, recent high energy electron irradiation studies and first-principles total-energy calculations are summarized and a defect induced by 7 MeV electron irradiation is identified.

1. Both N and Ga atoms are expected to be displaced from the lattice by 7-MeV electrons. To get $\tau = 1.2$ cm^{-1} in this study, we would require from the calculation of the relativistic cross section $\sigma(E)$ for atomic displacement as a function of electron energy E [32] and the lattice density of each of the atomic spices N_0 $(=\tau/\sigma(E))$, the energy necessary to create an N or Ga Frenkel (vacancy-interstitial) pair is about E_d(N)=8.8 eV or E_d(Ga)=30 eV. E_d(N) is lower than E_d(Ga) and this tendency agrees with those by Look *et al.* [11]. If we consider a specific property of GaN, a large mismatch in the covalent radii of Ga (r_{Ga}=1.26 Å) and N (r_{N}=0.75 Å) [38], the probability of irradiated electrons into collision with Ga atoms is larger than that of N atoms. Thus, it is difficult to conclude a primarily displacement (N or Ga) occurred in the electron irradiated GaN from only the energies E_d necessary to displace atoms.

2. Recent state of the art first-principles total-energy calculations [38, 39] have predicted the N vacancy (V_{N}) is a single shallow donor and the N interstitial (N_I) is a single deep acceptor around 1 eV from the top of valence band. On the other hand the Ga vacancy (V_{Ga}) is a single donor and the Ga interstitial (Ga_I) is a *triple* acceptor around 0.3 eV from the top of valence band. The energy levels of defects associated with N and Ga atoms is shown in Fig. 4.11. Thus, in order to obtain the electron irradiation dose dependence of carrier concentration n as shown in Fig. 4.9, a Ga Frenkel-pair model is consistent with this experimental result and proposed model discussed earlier. For an N Frenkel pair, however, the electron concentration n is independent of the electron irradiation dose.

Based on above discussion, a Ga Frenkel-pair model is tentatively the most likely defect induced by 7 MeV electron irradiation. The yellow-to-UV intensity ratio increases with increase in a Ga Frenkel-pair by increasing electron irradiation dose. Assuming that these reasonable interpretations are correct, the broad linewidth of yellow luminescence band is due to a radiative transition from a donor associated with a Ga_I at 0.93 eV [12] below the bottom of conduction band [10] or/and a shallow donor associated with a V_{N} to an acceptor associated with a $V_{\mathrm{G}a}$ at 0.3 eV [39] above top of valence band associated with a Ga vacancy.

However, further study is necessary to conclude the deep defect state model.

4.6 Conclusions

In this chapter, the detailed discussion of ESR properties of as-grown and electron irradiated hexagonal n-type GaN on sapphire substrate were presented. An single resonance at $g_{\parallel} = 1.9545$ and $g_{\perp} = 1.9451$ due to delocalized electrons in the conduction band or in a shallow impurity band was observed.

From the five-band $\mathbf{k}\cdot\mathbf{p}$ model using g value measured in this study, the matrix elements coupling between Γ_1 conduction and Γ_6 valence and its conduction bands, and spin-orbit splitting of the Γ_6 were estimated.

Low-temperature ESR linewidth decreased (narrowing) $T \leq T_{min}$ and increased (broadening) $T \geq T_{min}$ with increasing temperature (T). The mechanism of linewidth narrowing was due to an averaging of nuclear hyperfine structures with lattice nuclei through motion of the electrons (hopping conduction) and its broadening was due to an electron-phonon interaction.

The theoretical model based on rate equations were developed to investigate the change of UV-to-yellow luminescence ratio with changing 7 MeV electron irradiation dose. The model successfully predicted the experimental results in terms of a defect concentration and a carrier concentration.

To overcome a low sensitivity of conventional ESR, the low-temperature LESR was introduced to detect deep defect states. The numerical difference between the illuminated and dark conditions revealed no deep defect state except the resonance due to delocalized electrons in the conduction band or in a shallow impurity band. However, based on this study, reports according to high energy electron irradiation in GaN and the first-principles calculations, the change of the intensity ratio was due to the Ga Frenkel-pair with the energy necessary to create a Ga Frenkel $E_d = 30$ eV induced by high energy electron irradiation. And the yellow luminescence was tentatively identified to be a radiative transition from a donor band to a V_{Ga} acceptor.

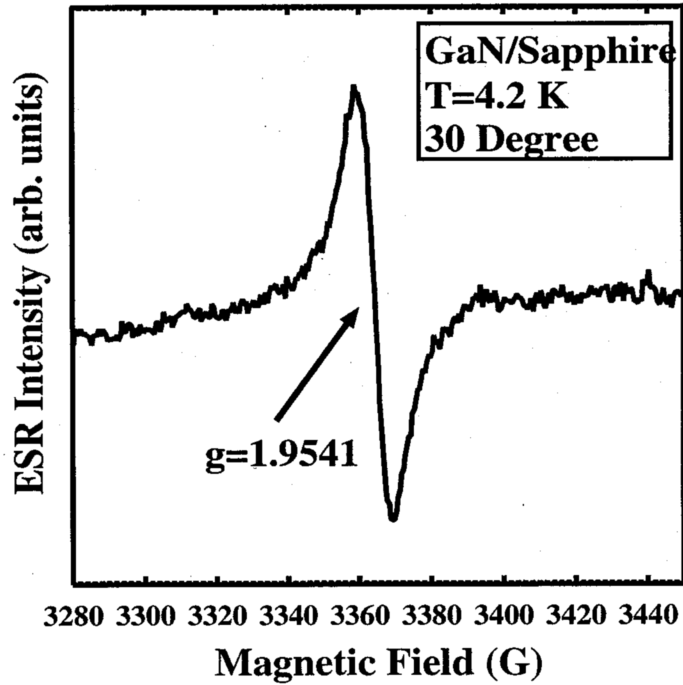

(a) The ESR signal measure at 30 degree from c-axis || magnetic filed.

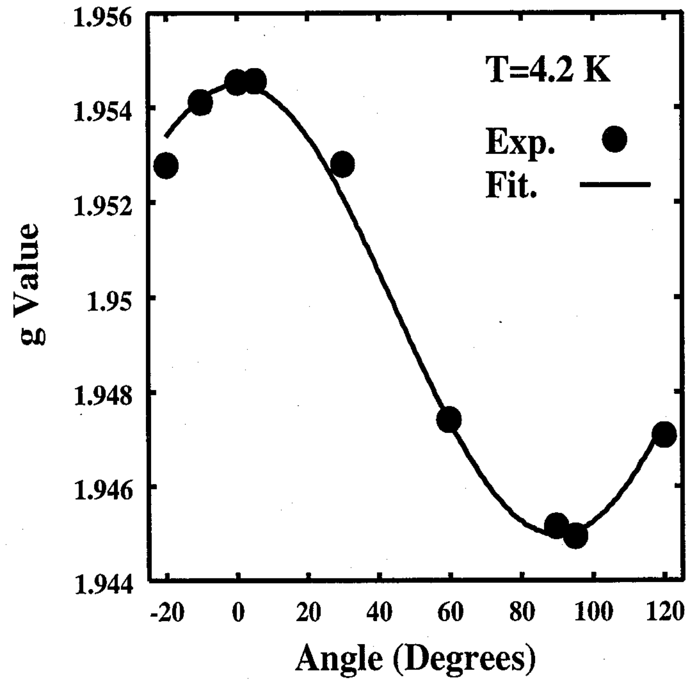

(b) The angular dependence with respect to c-axis.

Figure 4.1: The ESR signal and angular dependence for 4 μm n-GaN film sapphire substrate.

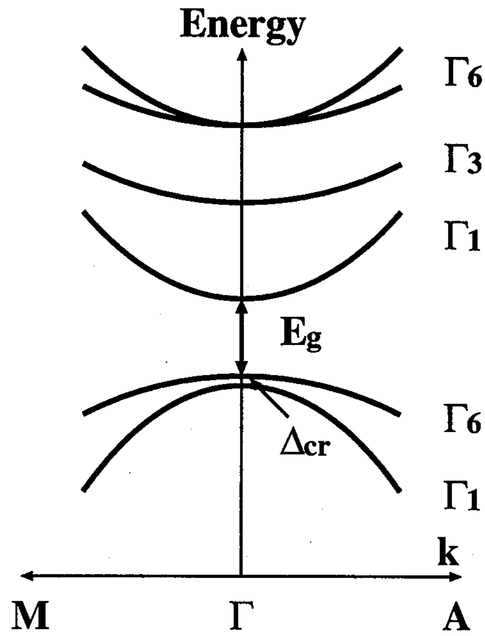

(a) The electron band structure of hexagonal GaN at Γ point. The energy spacing and band curvature are not to scale.

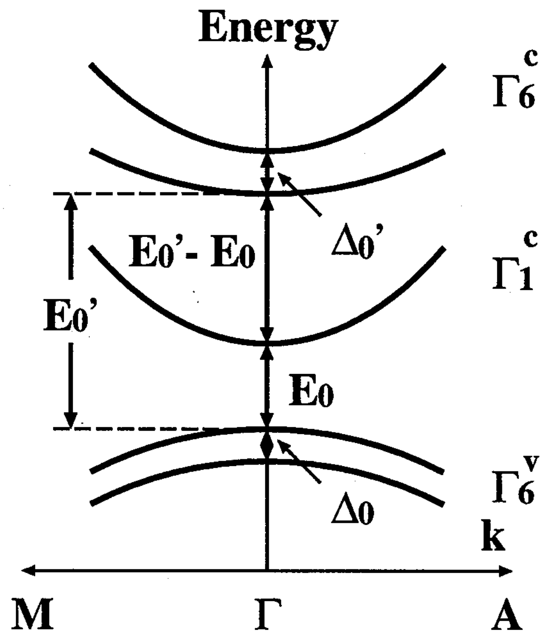

(b) The electron band structure of hexagonal GaN at Γ point. The energy spacing and band curvature are not to scale.

Figure 4.2: The electron band structure of hexagonal GaN.

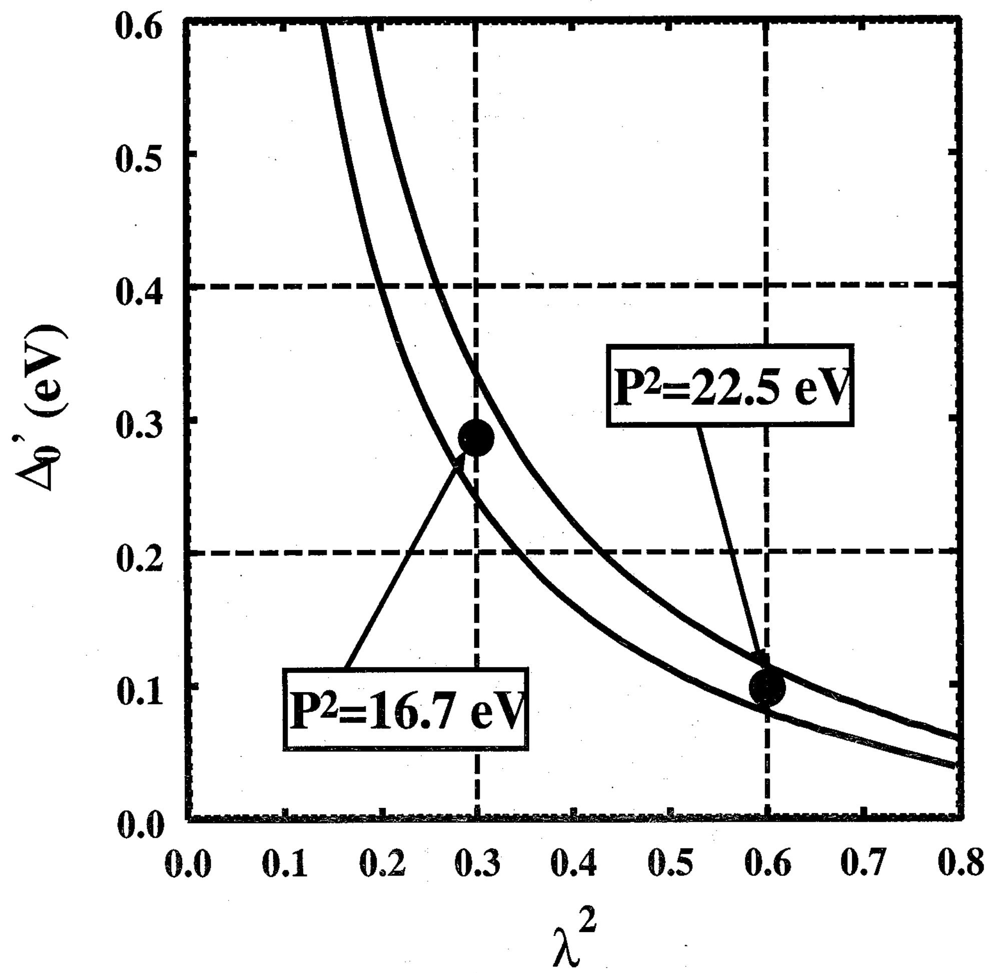

Figure 4.3: The calculated spin-orbit interaction Δ_0' as a function of λ^2.

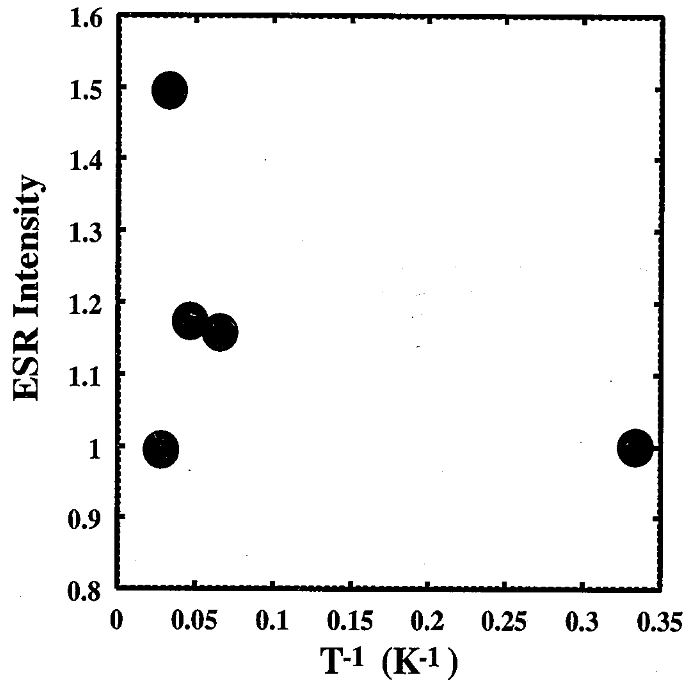

(a) The ESR intensity as a function of reciprocal temperature.

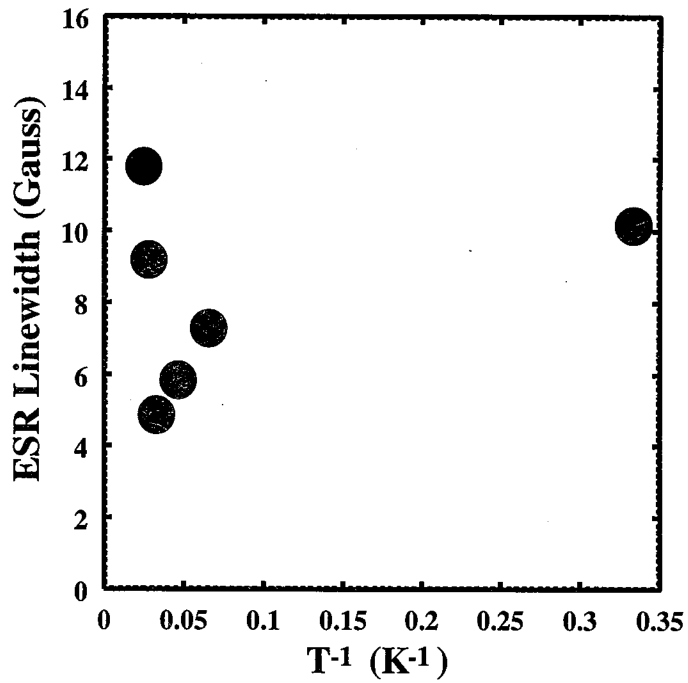

(b) The ESR linewidth (ΔH_{PP} as a function of reciprocal temperature.

Figure 4.4: The ESR signal characteristics of 4μm n-GaN film on sapphire substrate as a function of reciprocal temperature.

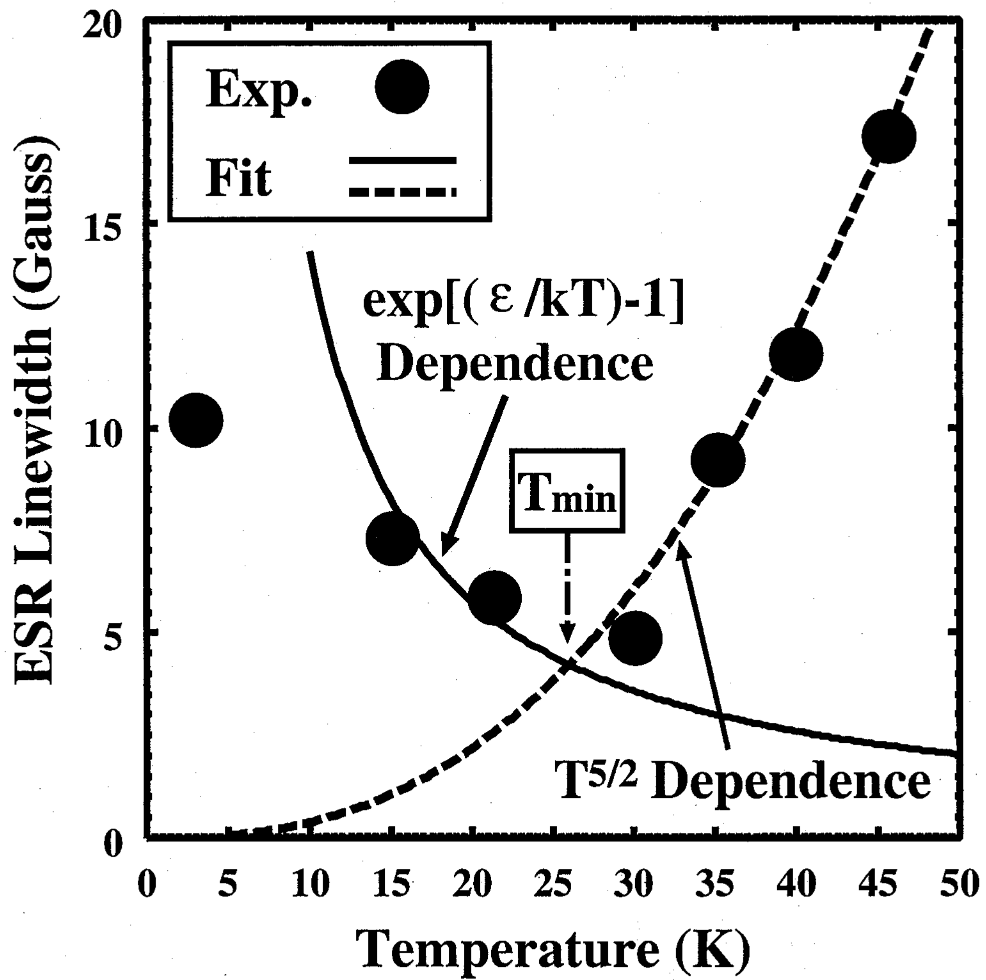

Figure 4.5: The linewidth of 4μm n-GaN film on sapphire substrate as a function of temperature. The solid line is a ($\exp(\varepsilon_3/kT) - 1$) fit to the experimental data below 25 K. The dashed line is a $T^{5/2}$ fit to the experimental data above 25 K.

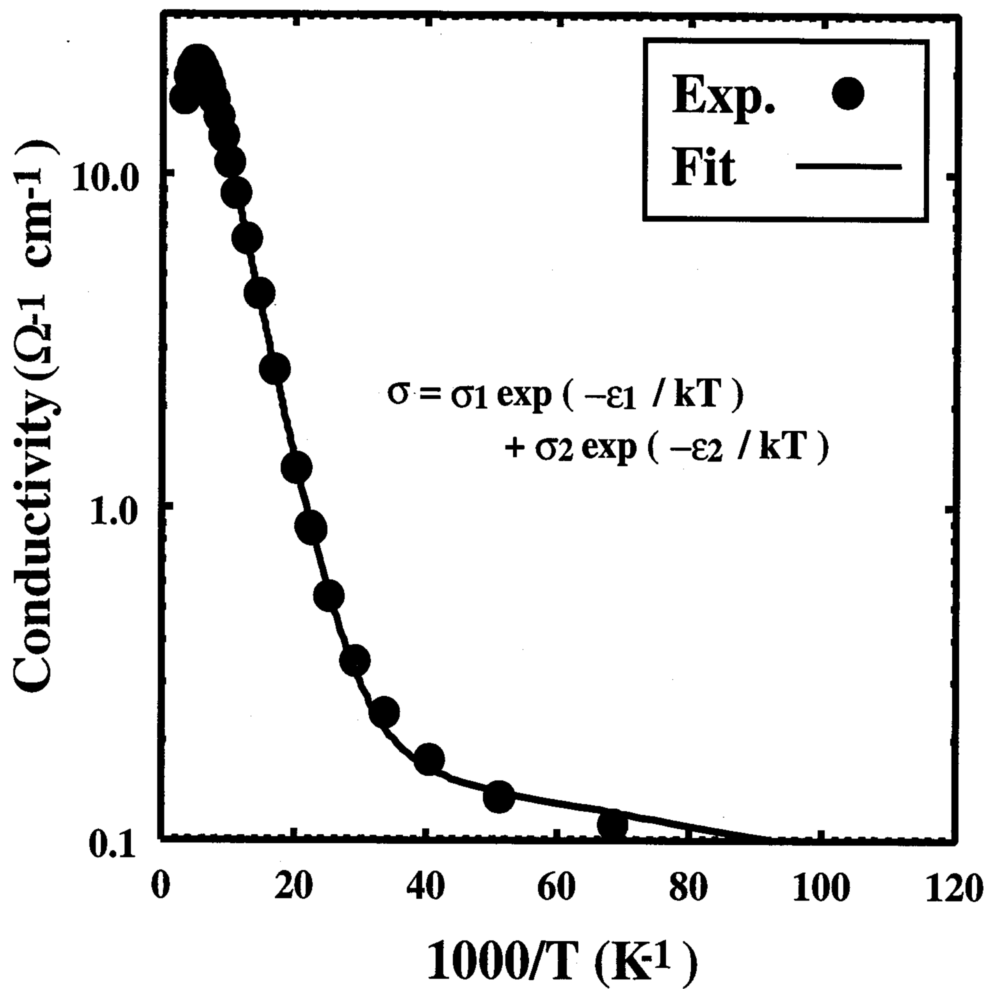

Figure 4.6: Conductivity of 2.4μm n-GaN on sapphire substrate as a function of $1000/T$.

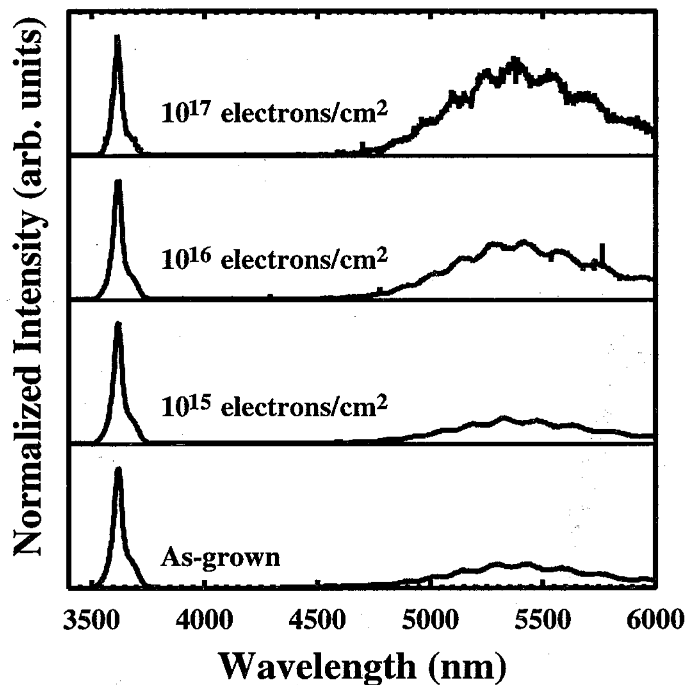

(a) Room-temperature photoluminescence spectra of as-grown and irradiated samples. The luminescence intensity is normalized to near-band-edge emission (~ 3.4 eV) intensity.

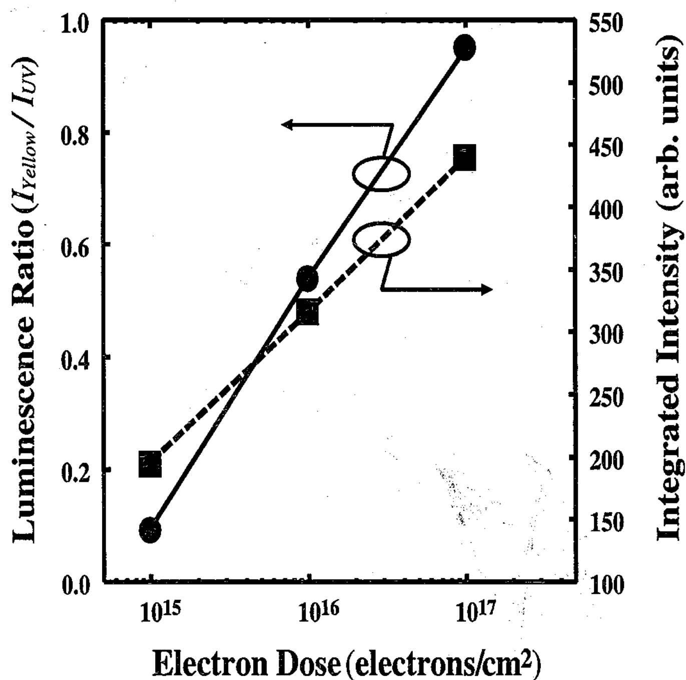

(b) Intensity ratio of the ultraviolet (UV) and yellow luminescence and integrated intensity of yellow luminescence as a function of electron irradiation dose.

Figure 4.7: Room-temperature photoluminescence spectra and its intensity characteristics.

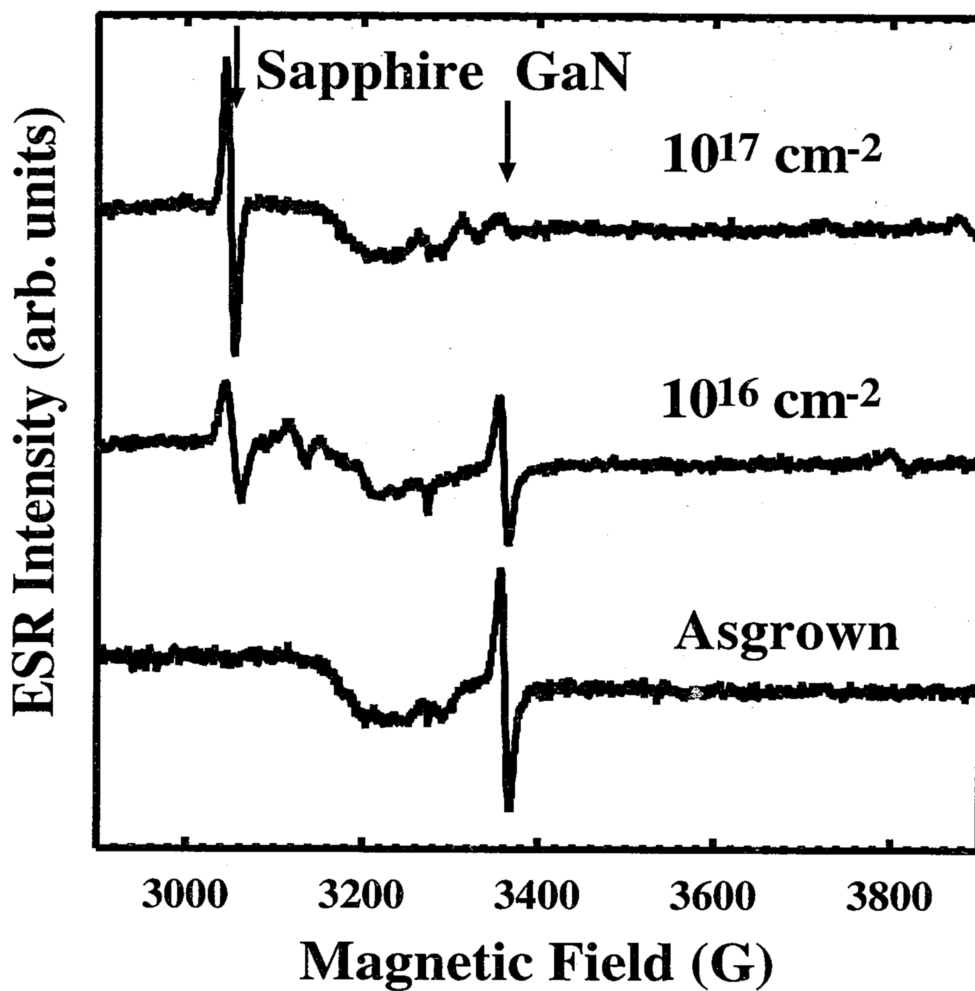

Figure 4.8: 4.2 K ESR spectrum for as-grown and electron irradiated n-GaN.

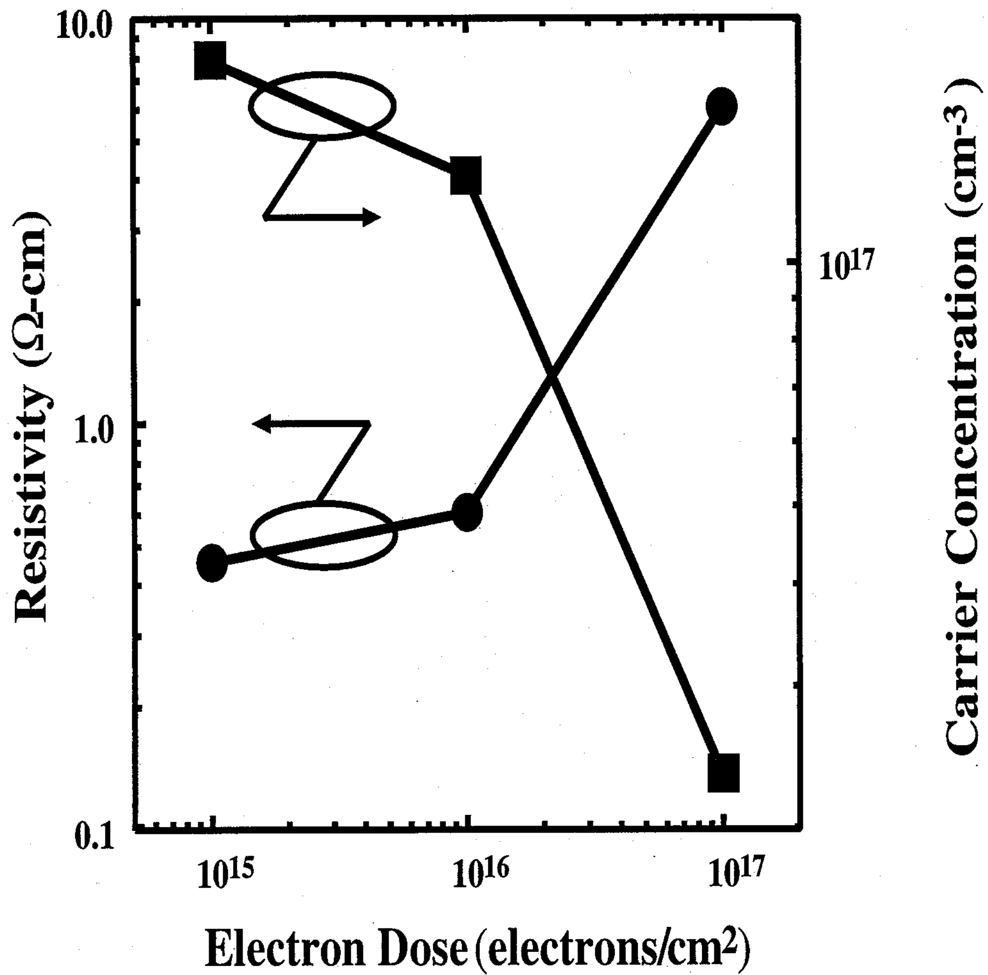

Figure 4.9: Resistivity and carrier concentration obtained by Hall measurements at 300 K as a function of electron irradiation dose.

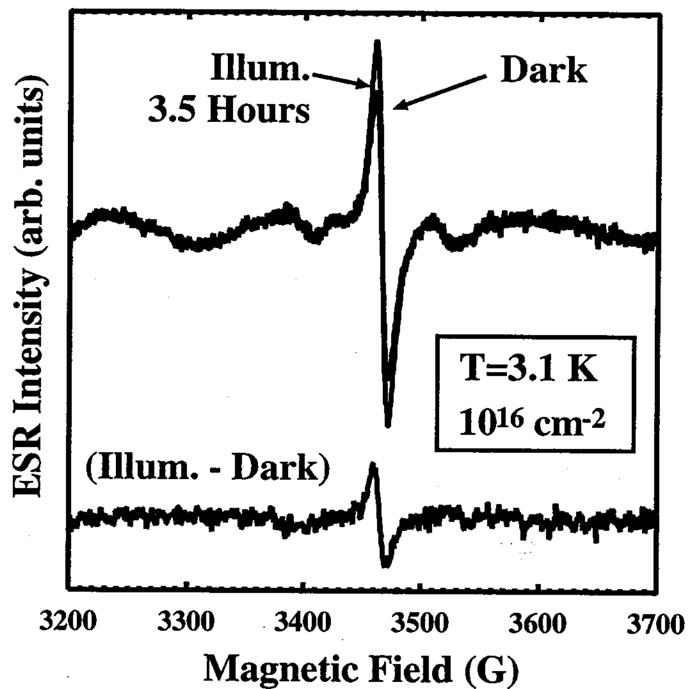

(a)

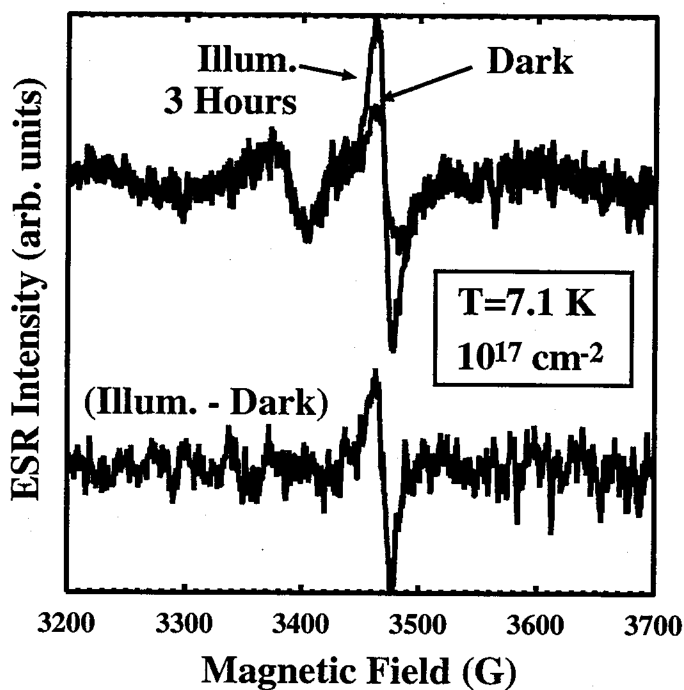

(b)

Figure 4.10: ESR spectra of the electron irradiated n-GaN at low temperature in the dark and under illumination. The bottom in each plot is the numerical difference spectrum (illumination - dark).

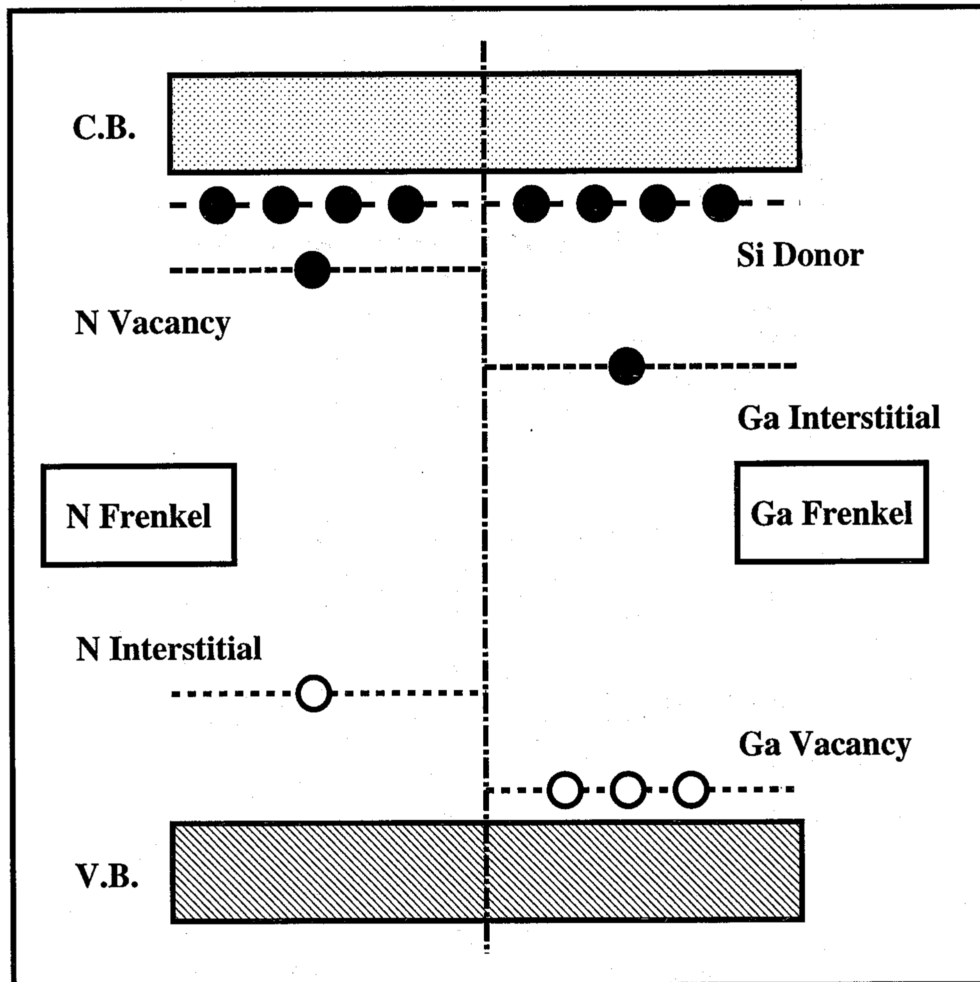

Figure 4.11: Schematic representation of the location of defect levels for the Ga and N vacancies and interstitials.

Bibliography

[1] H. Amano, M. Kito, K. Hiramatsu and I. Akasaki: Jpn. J. Appl. Phys. **28** (1989) L2112.

[2] I. Akasaki, H. Amano, Y. Koide, K. Hiramatsu and N. Sawaki: J. Cryst. Grwoth **98** (1989) 209.

[3] S. Nakamura, Y. Harada and M. Seno: Appl. Phys. Lett. **58** (1991) 2021.

[4] H. P. Maruska and J. J. Tietjen: Appl. Phys. Lett. **15** (1969) 323.

[5] W. Seifert, R. Franzheld, E. Butter, H. Sobotta and V. Riede: Cryst. Res. Technol. **18** (1983) 383.

[6] J. N. Kuznia, M. Asif Khan, D. T. Olson, R. Kaplan and J. Freitas: J. Appl. Phys. **73** (1993) 4700.

[7] G. D. Watkins and J. R. Troxell: Phys. Rev. Lett. **44** (1980) 593.

[8] D. Pons and J. C. Bourgoin: J. Phys. C **18** (1985) 1985.

[9] W. A. Barry and G. D. Watkins: Phys. Rev. B **54** (1996) 7789.

[10] M. Linde, S. J. Uftring, G. D. Watkins, V. Härle and F. Scholz: Phys. Rev. B **55** (1997) R10177.

[11] D. C. Look, D. C. Reynolds, J. W. Hemsky, J. R. Sizelove, R. L. Jones and R. J. Molnar: Phys. Rev. Lett. **79** (1997) 2273.

[12] Z. -Q. Fang, J. W. Hemsky, D. C. Look and M. P. Mack: Appl. Phys. Lett. **72** (1998) 448.

[13] M. AsifKhan, D. T. Olson and J. K. Kuznia: J. Appl. Phys. **74** (1993) 5901.

[14] D. Block. A. Heré and R. T. Cox: Phys. Rev. B **25** (1982) 6049.

[15] V. K. Bashenov: Phys. Status Solidi A **19** (1972) 9.

[16] R. Dingle, D. D. Sell, S. E. Stokowaski and M. Ilegems: Phys. Rev. B **4** (1971) 1211.

[17] D. E. Aspnse, C. G. Olson and D. W. Lynch: Phys. Rev. B **12** (1975) 2526.

[18] A. S. Barker, Jr. and M. Ilegems: Phys. Rev. **7** (1974) 676.

[19] R. Dingle, D. D. Sell, S. E. Stokowaski and M. Ilegems: Phys. Rev. B **4** (1971) 1211.

[20] S. Bloom, G. Harbeke, E. Meier and I. B. Orthenburger: Phys. Status Solidi B **66** (1974) 161.

[21] See C. Hermann and C. Weisbuch, in *Optical Orientation*, edited by F. Meier and B. P. Zakharchenya (North-Holland, Amsterdam, 1984), p. 463.

[22] R. R. L. Zucca and Y. R. Shen: Phys. Rev. B **1** (1970) 2668.

[23] B. Clerjaud, F. Gendron, H. Obloh, J. Schneider and W. Wilkening: Phys. Rev. B **40** (1989) 2048.

[24] M. Krapf, G. Denninger, H. Pascher, G. Weimann and W. Schlapp: Sloid State Commun. **74** (1990) 1141.

[25] G. Denninger, R. Beerhalter, D. Reiser, K. Maier, J. Schenider, T. Detchprohm and K. Hiramatsu: Sloid State Commun. **99** (1996) 347.

[26] S. Maekawa and N. Kinoshita: J. Phys. Soc. Jpn. **20** (1965) 1447.

[27] E. M. Gershenzon, N. M. Pevin and M. S. Fogelson: Phys. Status Solidi **38** (1970) 865.

[28] W. E. Carlos, J. A. Freitas, M .AsifKhan, D. T. Olson and J. N. Kuznia: Phys. Rev. B **48** (1993) 17878.

[29] M. Fanciulli, T. Lei and T. D. Moustaksa: Phys. Rev. B **48** (1993) 15144.

[30] N. F. Mott and W. D. Twose: Adv. Phys.**10** (1961) 107.

[31] A. Millerand E. Abrahams: Phys. Rev. **120** (1960) 745.

[32] R. Katz and A. S. Penhold: Rev. Mod. Phys. **24** (1952) 28.

[33] F. Agullo-Lopez, C. R. A. Catlow and P. D. Townsend: *Point Defects in Materials* (Academic, New York, 1998).

[34] A. Billeb, W. Grieshaber, D. Stocker, E. F. Schubert and R. F. Karicek, Jr.: Appl. Phys. Lett. **70** (1997) 2790.

[35] T. Ogino and M. Aoki: Jpn. J. Appl. Phys. **19** (1980) 2395.

[36] J. Neugebauer and C. G. Van de Walle: Appl. Phys. Lett. **69** (1996) 503.

[37] A. Hoffmann, L. Eckey, P. Maxim, J. -C. Holst, R. Heitz, D. Kovalev, G. Stevde, D. Volm, B. K. Myer, T. Dechprohm, K. Hiramatsu, H. Amano and I. Akasaki: Sloid-State Electron. **41** (1997) 275.

[38] J. Neugebauer and C. G. Van de Walle: Phys. Rev. B **50** (1994) 8067.

[39] P. Boguslawski, E. L. Briggs and J. Bernholc: Phys. Rev. B **51** (1995) 17255.

Chapter 5

Thermal Stress Reduction of GaAs Layer over Thin Si Layer on Porous Si Substrate

5.1 Introduction

Applying GaAs on Si substrate (GaAs/Si) technology to GaAs devices (electrical and optical devices) is significant for improving the characteristics of these devices by its high thermal conductivity and reducing their cost by its large diameter and mechanical hardness. This heterostructure is a very fashionable material for future optoelectronic devices like optoelectronic integrated circuits (OEICs) [1, 2] because of the possibility of combining the advantages of the individual materials. Although the heteroepitaxial growth of GaAs/Si has been received considerable attention, however, as discussed in chapter 1, the GaAs/Si have inherent problems due to the large lattice and thermal expansion coefficient different and high density of dislocation near the heterointerface and un-negligible residual thermal strain in epitaxial layers.

As for electronic device application, not only the discrete devices like high electron mobility transistors (HEMTs) [3, 4], metal semiconductor field effect transistors (MESFETs) [5, 6] and solar cells (SCs) [7, 8] but integrated circuits (ICs) [9, 10] have been successfully fabricated using the GaAs/Si and have reported to show comparable results to those on GaAs substrate.

On the other hand, however, as for optoelectronic device application like light emitted diodes (LEDs) [11] and laser diodes (LDs) [12, 13] have made slow progress. The performance and reliability of these devices fabricated on GaAs/Si are less comparable to those fabricated on GaAs substrate especially in lifetime. This indicated that the problems of dislocation and residual stress drastically affect the performances of optoelectronic device compared to those of electronic devices [14].

The problems caused by lattice mismatch have been solved by using a low-temperature GaAs buffer layer (two-step growth technique [15]). However, thermal stress can hardly be avoided in heteroepitaxial structures. The reduction of thermal stress is key issue in wide spread of GaAs/Si technology. There have been demonstrated the reduction of thermal stress by using the selective-area growth [16], the post-growth patterning [17, 18]. These methods are based on the facts that the residual thermal stress and the defect density are decrease with reduction of the growth area. Another approach to reduce the thermal stress is proposed by using an undercut GaAs mesa structure [19], an epitaxial layer over-growth [20] and direct wafer bonding technique [21]. Approaches are summarized in Fig. 5.1.

Although many ideas have been proposed to overcome the problems lying on GaAs/Si the decisive procedure has not reported yet. In this chapter, new thin Si Layer over porous Si (SPS) substrate instead of the conventionally used Si substrate will be proposed to overcome especially

the residual thermal stress in GaAs/Si.

This new idea is based on the thin Si layer that is weakly bonded to bulk Si substrate via the porous regions of the Si substrate. Because of the thin Si layer (the thickness of GaAs is much greater than that of the thin Si layer) the thermal strain introduced during cooling after the growth is easily absorbed by the porous regions.

In this chapter, the new approach to overcome the residual thermal stress in GaAs/Si will be discussed. To the best of my knowledge, this idea has never been reported yet.

5.2 Similar Study

The similar study in which the initial stage of GaAs layer was grown directly on a porous Si by molecular beam epitaxy (MBE) has been reported by Hasegawa *et al.* [22]. However in this report, they did not use of a thin Si layer over porous region which is very different from this proposed idea. And they concluded that the porous Si was a promising candidate for obtaining GaAs with good quality on Si substrate. Prior to introduce the new idea, the growth of GaAs directly on porous Si substrate was performed, however, it was not successful at all. Because of much differences in wafer preparation and growth condition (MBE/MOCVD, temperature, etc.), it is difficult compare this study with theirs at this time.

5.3 Preparation of Porous Si Wafer

A thin Si layer over porous Si substrate was proposed for developing new silicon-on-insulator (SOI) by Yonehara *et al.* and co-workers at Canon Inc. [23, 24, 25]. They found that the defect (the major defects are stacking faults) density in the epitaxial Si layers over porous region can be reduced to 3.5×10^2 cm^{-2}by raising the H_2 prebake temperature and in conjunction with the "preinjection technique" in which a small amount of Si is supplied during the high-temperature H_2 prebake prior to epitaxial growth. The reduction of defects is very important to realize a good quality of GaAs over thin Si layer.

A 12-μm-thick porous Si surface layer was formed by the anodization method. The porous Si layer was slightly oxidized in O_2 ambient at 400°C. After removing the low-temperature oxide on the surface, the Si epitaxial layer around 10 nm was grown at 1060°C by chemical vapor deposition after hydrogen prebaking to seal the pores [25]. The SPS substrate was prepared at Canon Inc.

5.4 Epitaxial Growth of GaAs

The substrates were rinsed in organic solvents and then cleaned in solutions of H_2SO_4 (4:1 by volume) and HF:H_2O (1:1 by volume). The cleaning time was modified to avoid removing all thin Si epitaxial layer ($\approx$ 10 nm) over porous region.

The GaAs was grown using atmospheric pressure MOCVD with rf-heated horizontal reactor. Trimethylgallium (TMG) was used as a group-III source, and arsine (AsH_3) was used as a group-V source. The carrier gas was hydrogen (H_2). After loading the substrate into the reactor, the substrate was heated at 1000°C for 10 min in a hydrogen ambient. In this study, the conventional two-step growth technique, where the initial stage of GaAs nucleation layer was grown at 400°C and then the temperature was raised at 750°C to grow a 3-μm-thick undoped GaAs layer, was used.

In this study, the thermal cycle annealing (TCA), which improves the crystal quality, was not performed.

5.5 Characterization Details

After GaAs epitaxial growth, scanning electron microscope (SEM), low temperature photoluminescence (PL), double-crystal X-ray diffraction (XRD) and Micro–Raman scattering measurements were performed to identify the effect of proposed idea in comparison with a general GaAs/Si.

SEM was used to know the schematic cross-section of GaAs epitaxial film grown on SPS substrate.

The X-ray rocking curves using Cu $K\alpha$ radiation were recorded in the vicinity of symmetric (004) reflection by Rigaku double-crystal diffractometer. From (004) reflection, the lattice constant perpendicular to GaAs(001) plane ($a_\perp$) were determined.

Low-temperature PL measurements were done at 4.2 K. The samples were excited by an argon ion (Ar^+) laser operated at 514.5 nm. The photoluminescence signals were separated by a monochromator and were detected by a photomultiplier.

Room-temperature Micro–Raman scattering measurements were performed precisely using triple-grating spectrometer with a liquid nitrogen-cooled charge coupled device (CCD) array. A 10 mW, 514.5 nm, Ar^+ laser was used as the light source. A 50× objective was employed, giving a laser-illuminated spot of 1.0 to 1.5 microns in diameter, and a resolution was 0.10 cm^{-1}. The measurements were performed in back scattering $z(yy)\bar{z}$ geometry where the polarization of the incoming incident light was perpendicular to the GaAs epitaxial layer and the scattered light was unpolarized. The wavenumber was calibrated by the use of a neon lamp. Because the measurement was performed back scattering geometry, only the LO phonon mode was allowed from a GaAs(001) surface due to the selection rules for the first-order Raman scattering.

5.6 Experimental Results and Analysis

Scanning Electron Microscope Analysis:

The schematic cross-section and scanning electron microscope (SEM) micrograph of GaAs on SPS are shown in Figs. 5.2(a) and 5.1(b),respectively. The thickness of porous Si is about 12 μm. Even after thermal cleaning at 1000°C before growth, it is clearly seen that the thin Si layer on porous region still remains on the porous regions. The GaAs surface is cloudy in both GaAs/Si and GaAs/SPS and these results are due to anti-phase domain (APD) due to the polar (GaAs)-nonpolar (Si) material system. In general, APD has been already solved by use of nominally (100)-oriented Si substrate with a slight misorientation between 2° and 6° towards the [011] direction [26, 27].

Double-crystal X-ray Diffraction Analysis:

The residual thermal stress was first analyzed by XRD. The distances between (004) lattice planes of Si and GaAs are determined by the Bragg diffraction conditions

$$2d_{\mathrm{Si}(004)} \sin\theta_{\mathrm{Si}(004)} = \lambda, \tag{5.1}$$

$$2d_{\mathrm{GaAs}(004)} \sin\theta_{\mathrm{GaAs}(004)} = \lambda, \tag{5.2}$$

where λ is the wavelength of the X-ray (Cu Kα line; λ = 1.540562 Å) and $\theta_{\mathrm{Si}(004)}$ and $\theta_{\mathrm{GaAs}(004)}$ are the Bragg angle of the Si and GaAs (004) reflections, respectively. The distances between (004) lattice planes of GaAs $d_{\mathrm{GaAs}(004)}$ are reduced to

$$d_{\mathrm{GaAs}(004)} = \frac{\lambda}{2\sin\left(\theta_{\mathrm{Si}(004)} - \Delta\theta_{(004)}\right)}, \tag{5.3}$$

where $\Delta\theta$ is the reflection peak separation between Si and GaAs which is given by

$$\Delta\theta_{(004)} = \theta_{Si(004)} - \theta_{GaAs(004)}. \tag{5.4}$$

The lattice constant perpendicular to GaAs(001) is determined by

$$a_{\perp} = \mathrm{d}_{(h,k,l)}\sqrt{\mathrm{h}^2+\mathrm{k}^2+\mathrm{l}^2}. \tag{5.5}$$

Thus, $a_{\perp}$ of GaAs on Si substrate is determined only from the reflection peak separation between Si and GaAs of XRD result.

If the lattice of GaAs/Si epitaxial layer is very perfect, its elastic property would be the same as that of bulk GaAs. The strain parallel to the (001) $\varepsilon_{\parallel}$, which is in-plane strain, is calculated according to the elastic theory given by

$$\varepsilon_{\parallel} = -2\frac{C_{12}}{C_{11}}\varepsilon_{\perp}, \tag{5.6}$$

where C_{ij} are the elastic stiffness coefficients and $\varepsilon_{\perp}$ (= $\mathrm{a}_{\mathrm{bulk\ GaAs}}$ - $\mathrm{a}_{\perp}$, where $\mathrm{a}_{\perp}$ is the lattice constant perpendicular to (001)) is the strain of GaAs perpendicular to the (001) plane. The stress parallel to the (001) $\sigma_{\parallel}$ which is in-plane stress was calculated by

$$\begin{aligned} \sigma &= -\frac{E}{1-\nu}(2\frac{C_{12}}{C_{11}})\varepsilon_{\perp} \\ &= \frac{E}{1-\nu}\varepsilon_{\parallel}, \end{aligned} \tag{5.7}$$

where ν is the Poisson ratio of the GaAs.

Figure 5.3 shows the XRD (004) reflection patterns of Si and GaAs. It is evident that the GaAs-Si peak separation of GaAs/SPS is larger than that of GaAs/Si. In this case, this result indicates that the GaAs lattice of GaAs/SPS is relaxed compared that of GaAs/Si. From the XRD results, the full width at half maximum (FWHM) of the rocking curves and the calculated residual stress in GaAs layer are summarized in Table 5.1. The broader FWHM (by 21 arcsec) of GaAs/SPS compared to that of GaAs/Si indicates that the crystal quality is worse because the FWHM of XRD peaks is related to the distortion of lattice parameters. The details will be discussed later. Though the crystallinity became worse based on FWHM results, a decrease of the residual stress in the GaAs layer is observed clearly using the SPS substrate.

Photoluminescence Analysis:

Three distinct emissions in both GaAs/Si and GaAs/SPS from PL measurements was observed, as shown in Figs. 5.4(a) and 5.3(b). The emissions around 830 and 835 nm (which are denoted as peak A and B) are the intrinsic transitions between the conduction band and the valence band. Under biaxial tensile strain, the valence band is split into heavy-hole (hh) and light-hole (lh) bands. Thus, A and B are emission peaks resulting from the 'lh' and the 'hh' transitions. The peak A is weak because the selection rule prohibits the emission of photons in the direction perpendicular to the surface. The peak at around 845 nm (which is denoted as peak C) originates from the neutral-carbon-related free-to-bound recombination. (As is well known, the carbon is dominant residula impurity acting as an acceptor in GaAs.)

The shift in the energy difference (ΔE_{hh}) between the conduction band and the heavy hole (E_{hh}) and light hole (E_{lh}) bands relative to the unstrained energy difference as a function of strain (ε) are given by [28, 29]

$$\Delta E_{hh} = \left(-2a\frac{C_{11}-C_{12}}{C_{11}} - b\frac{C_{11}+2C_{12}}{C_{11}}\right)\varepsilon, \tag{5.8}$$

$$\Delta E_{lh} = \left(-2a\frac{C_{11}-C_{12}}{C_{11}} + b\frac{C_{11}+2C_{12}}{C_{11}}\right)\varepsilon, \tag{5.9}$$

where a is a hydrostatic deformation potential and b is a shear deformation potential. For the case of GaAs, these parameters have values of C_{11}=122.6 GPa, C_{12}=57.1 GPa, $a = -6.0$ eV and

$b = -2.0$ eV. Then, the stress in the GaAs from the relationship between strain (ε) and stress (σ) using Young's modulus ($E = 85.3$ GPa). ($\sigma = E \cdot \varepsilon$)

The spectrum of GaAs/SPS is similar to GaAs/Si but is shifted to the higher energy region by 2.7 meV. The estimated residual strains are 2.9×10^{-3} and 2.6×10^{-3} for GaAs/Si and GaAs/SPS, respectively. The calculated stress at 4.2 and 300 K are summarized in Table 5.2. The values ε_0 at T_0=300 K were estimated from the first-order approximation of $\varepsilon(T) = \varepsilon_0 - \Delta\alpha(T - T_0)$, where $\Delta\alpha$ is the difference in the thermal expansion coefficient between α_{GaAs} and α_{Si}.

At room temperature, the residual stress decreases from 0.18 to 0.15 GPa.

Micro-Raman Analysis:

Raman scattering experiments were carried out in the backscattering geometry; therefore, the LO phonon mode is allowed from a GaAs(001) surface due to the selection rules for the first-order Raman scattering. Figure 5.5 shows Raman spectra of GaAs layer grown on GaAs, Si and SPS substrates.

The crystal quality and the stress are determined from the FWHM and the frequency shift of the longitudinal optical (LO) phonon line. The strain σ along (100) for the backscattering produces the LO phonon frequency shift. The relationship between the stress (σ) and phonon shift is expressed as [30]

$$\sigma = \frac{\omega^2 - \omega_0^2}{p \cdot (S_{11} - S_{12}) + q \cdot (S_{11} + 3S_{12})}, \tag{5.10}$$

where ω and ω_0 (= 291.63 cm^{-1}) are the strained and unstrained LO phonon frequencies, S_{ij} is the elastic compliance constant and p and q are the dimensionless phonon deformation potential for LO phonon. The values used in this calculation are summarized in Table 5.3.

The frequency shifts of GaAs/Si and GaAs/SPS are about 1.0 and 0.2 cm^{-1}, respectively, in comparison with that of GaAs/GaAs, and the magnitude of the stress are estimated to be, respectively, 0.279 and 0.050 GPa. The internal strain reduction is confirmed also by Raman scattering measurement. The results of Raman scattering are shown in Table 5.4.

The FWHM of phonon line is related to the phonon lifetime and the fluctuation of a spring constant between Ga and As atoms. Thus, the crystal quality in terms of FWHM of GaAs/SPS is worse than that of GaAs/Si.

5.6.1 Film quality and stress relaxation

The estimated value of strain of GaAs/SPS from XRD agreed with that obtained from the PL peak shift. However, the estimated value of strain from Raman scattering is smaller than those obtained from XRD and PL results. This may be due to the light (Ar^+ 514.5 nm) penetration depth (D) of about 108.3 nm in the case of GaAs [31]. Figure 5.6 shows the probe area in GaAs epitaxial layer by photoluminescence, double-crystal X-ray diffraction and Raman scattering measurements. From this figure, Raman scattering measurements characterize only the very near surface portion of the GaAs layer. However, XRD characterize the entire inner portion of GaAs layer from the top surface. Also, PL measurements characterize nearly half ($\approx D+$ carrier diffusion length) of the GaAs layer from the top surface.

5.6.2 Stress relaxation mechanism

Up to now, the results of the stress (strain) reduction of GaAs layer by using SPS substrate are shown. The detail mechanism is not clear at this time; however, this may be due to the following technology and mechanisms. The key technology in this investigation is to use a thin Si layer on the porous region because growth of a GaAs layer directly on the porous region was not successful at all in the previous study. In spite of this result, Hasegawa *et al.* [22] reported that porous Si is a promising candidate for obtaining GaAs with good quality on Si substrate. Because of much different wafer preparations and growth conditions, it is difficult to compare these results with theirs at this time. In the combination of the thin Si layer with the porous region, the

residual thermal strain that is introduced during cooling from the growth temperature is easily absorbed by the porous regions by bending (bowing) the thin Si layer, and a high degree of stress relaxation in GaAs layer on SPS substrate. Thus, the lattices of GaAs epitaxial layer and Si substrate contract in accordance with individual (GaAs, Si) thermal expansion coefficients during cooling from the growth temperature, as shown in Fig. 5.7. It should be noted that the thickness of the SPS substrate (600 μm) is almost twice that of Si (340 μm). Thus, the data obtained here support the above-mentioned mechanism.

5.7 Conclusions

In conclusion, the new SPS substrate instead of the conventionally used Si substrate has proposed to over come the residual thermal stress in GaAs/Si. The GaAs film were characterized by low temperature photoluminescence (PL), double-crystal X-ray diffraction (XRD) and Micro–Raman scattering measurements and the stress reduction of GaAs layer on SPS substrate was successfully obtained. Results show that the significant reduction in the residual tensile strain in GaAs layer have been achieved by this method; however, the improvement of crystal quality in terms of FWHMs (XRD, PL and Raman scattering) of GaAs/SPS is still remained.

Compared to the selective-area growth or the post-growth patterning discussed in §5.1, this method is applicable to large areas of GaAs/Si.

Table 5.1: X-ray diffraction (XRD) results and the estimated stress in GaAs layer.

	GaAs/Si	GaAs/SPS
FWHM (arcsec)	205	226
Stress (GPa)	0.214	0.148

Table 5.2: Estimated stress at 4.2 and 300 K calculated based on the shifts in the energy difference between the conduction band and heavy hole band in low-temperature photoluminescence.

	GaAs/Si	GaAs/SPS
Stress (GPa)	0.25 (0.18)	0.23 (0.15)

Values inside parentheses indicate the stresses at 300 K estimated from those of 4.2 K.

Table 5.3: Dimensionless values p and q of phonon deformation potentials for LO phonon and elastic compliance constant S_{ij} (in units of 10^{-12} $dyn^{-1}cm^2$) for GaAs.

$S_{11} + 2S_{12}$	0.445
$S_{11} - S_{12}$	1.54
$[(p-q)/\omega_0^2]$	0.7 ± 0.03
$[-(p-q)/6\omega_0^2]$	0.1.23 ± 0.03

All values are from ref. [32].

Table 5.4: Raman scattering results of LO phonon and the estimated stress in GaAs layer.

	GaAs/GaAs	GaAs/Si	GaAs/SPS
Raman Shift (cm^{-1})[a)]	291.6	290.6	291.4
FWHM (cm^{-1})	7.8	7.9	9.5
Stress (GPa)	0.00	0.28	0.05

[a)] Raman shifts were derived from a fitting assuming the Lorentzian line shape.

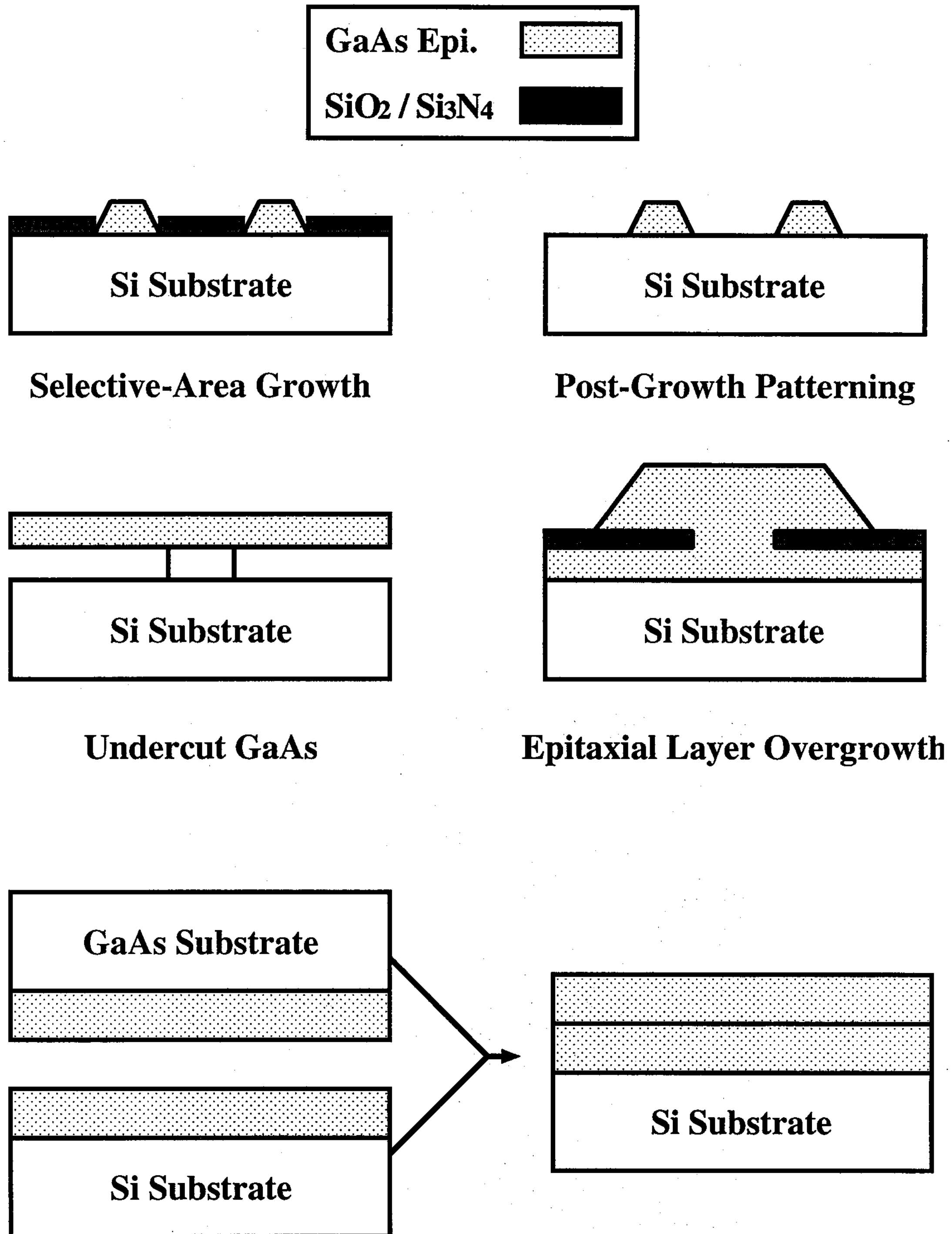

Figure 5.1: Several techniques to reduce the thermal stress and associated dislocations.

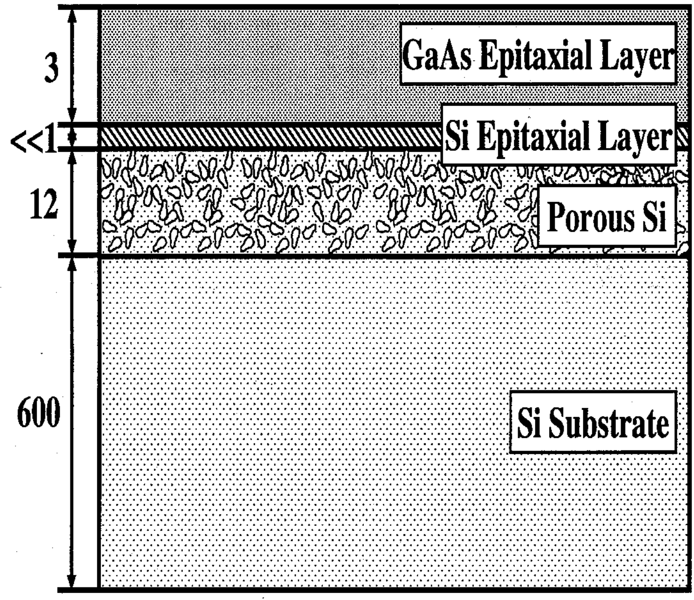

(a) Cross sectional image of GaAs/SPS.

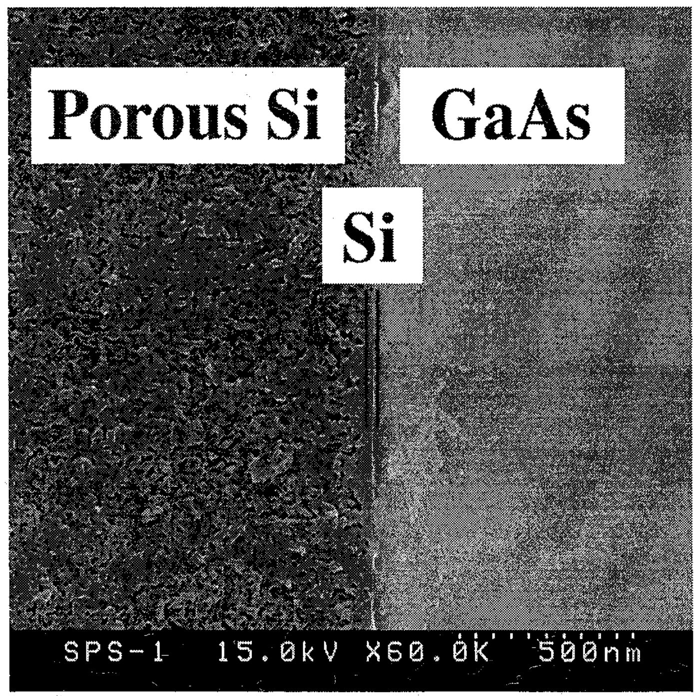

(b) Cross sectional SEM micrograph of the GaAs/SPS heterointerface.

Figure 5.2: Cross-sectional image of GaAs/SPS (a) and cross-sectional SEM micrograph of the GaAs/SPS heterointerface (b).

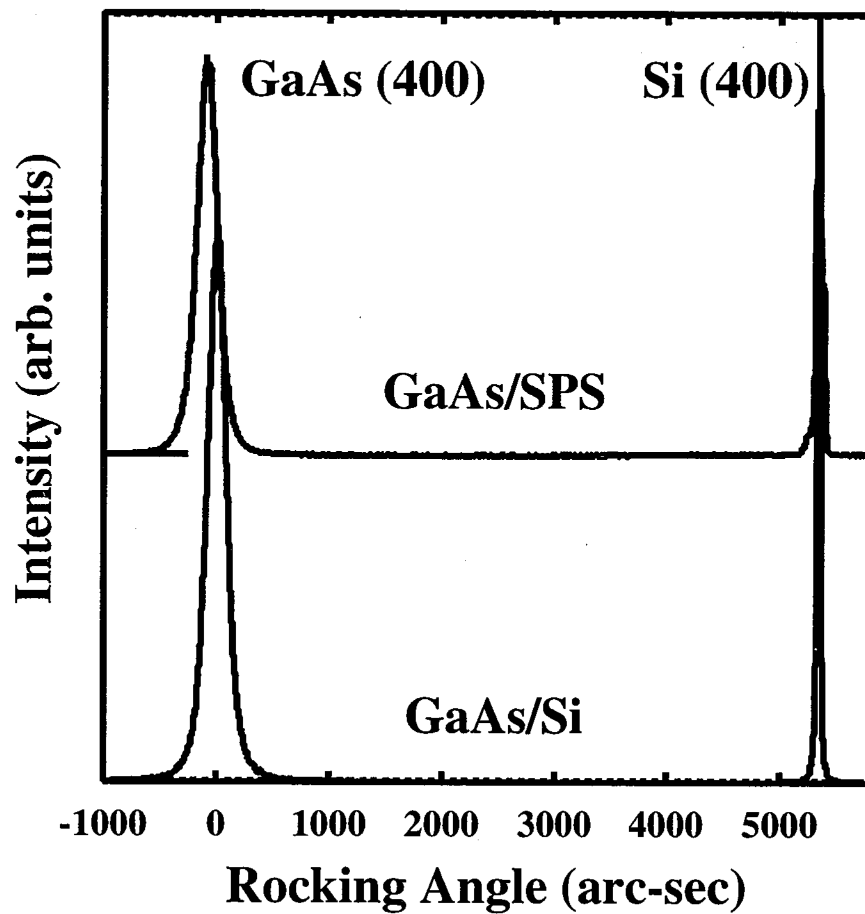

Figure 5.3: X-ray rocking curves for GaAs/Si and GaAs/SPS.

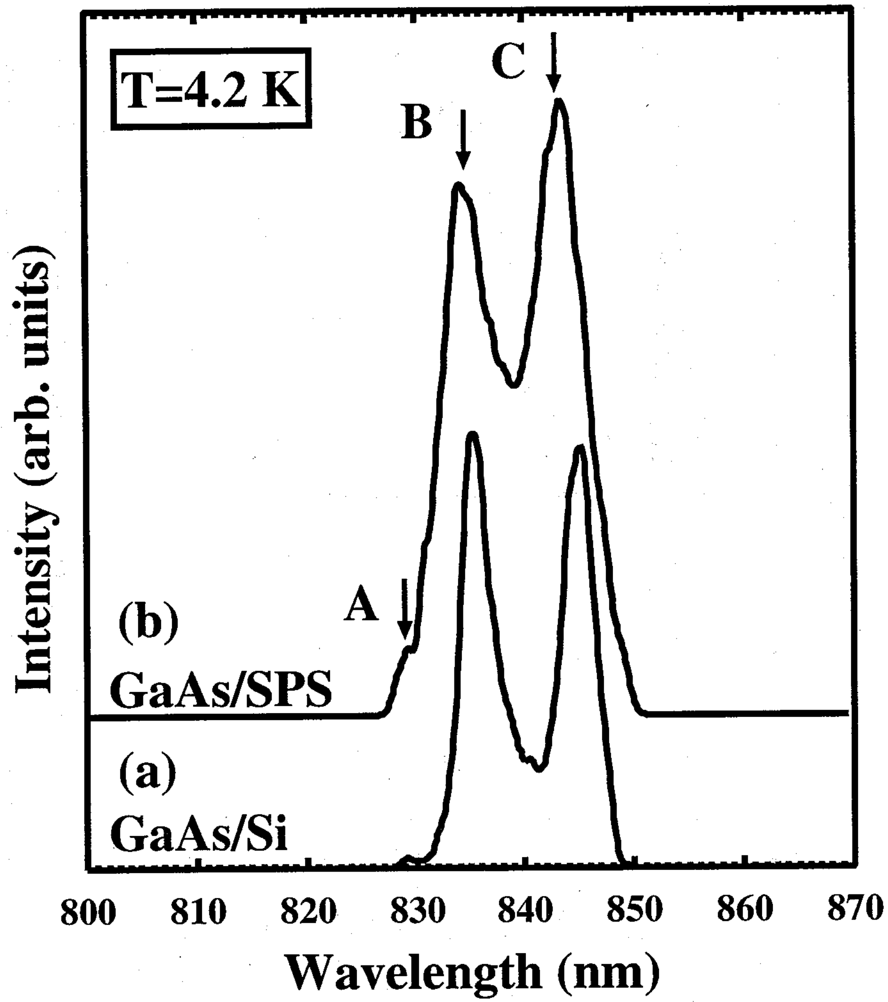

Figure 5.4: PL spectra at 4.2 K for GaAs/Si and GaAs/SPS.

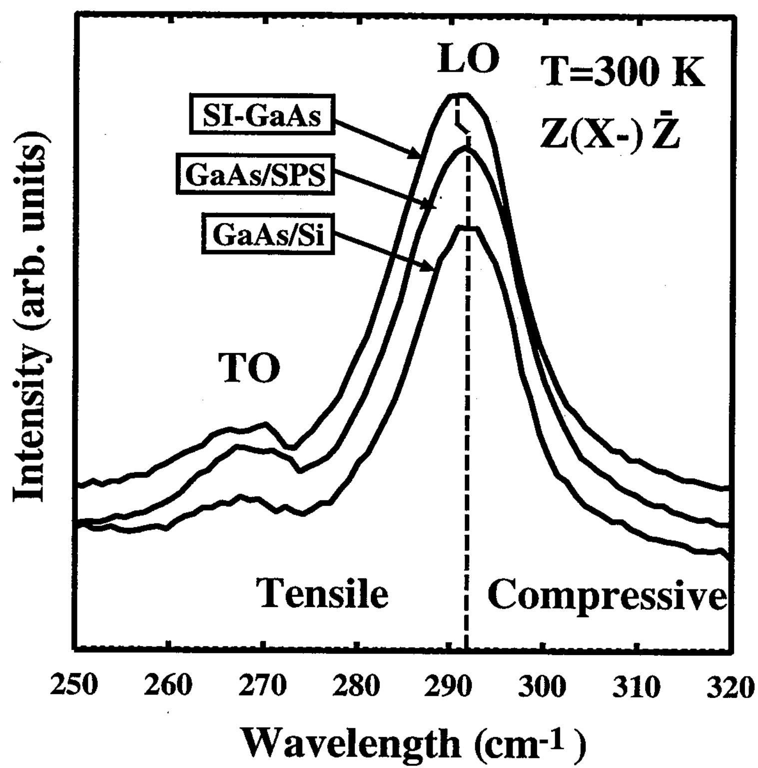

Figure 5.5: Raman spectra at 300 K for GaAs/Si and GaAs/SPS.

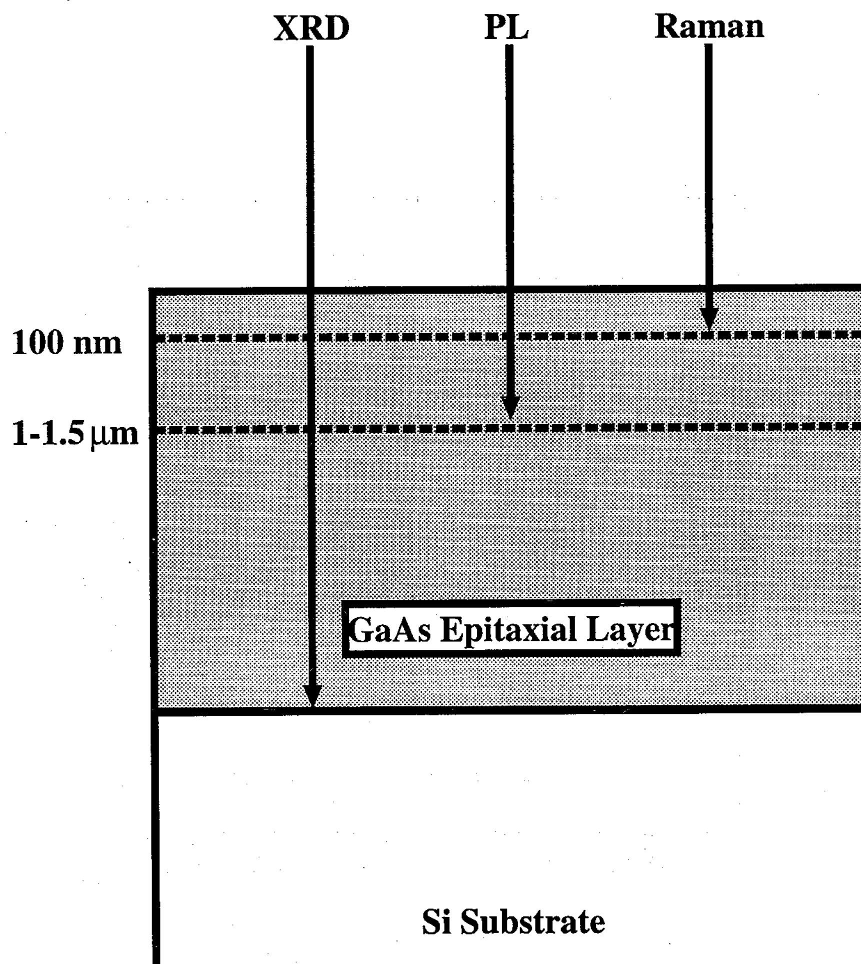

Figure 5.6: Probe area in the GaAs layer by X-Ray diffraction, PL and Raman scattering.

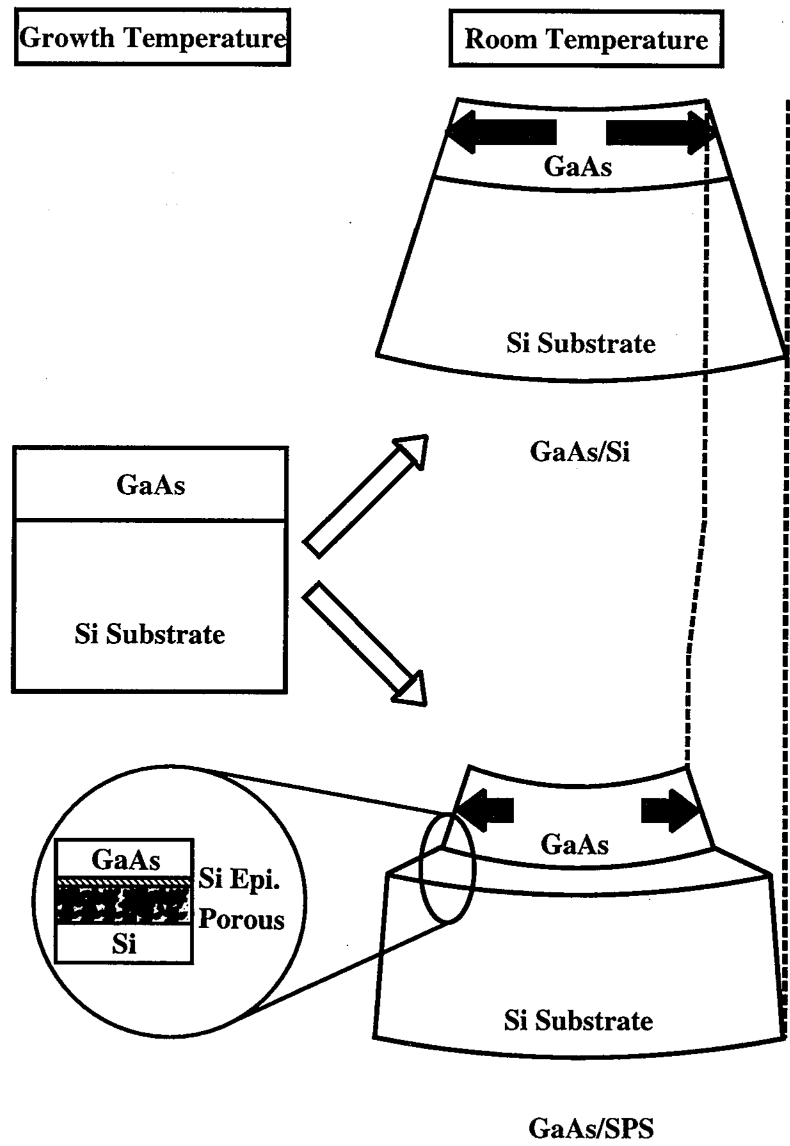

Figure 5.7: Thermal stress relaxation mechanisms for GaAs/Si and GaAs/SPS.

Bibliography

[1] H. K. Choi, J. P. Mattia, G. W. Turner and B. -Y. Tsaur: IEE Electron Device Lett. **9** (1988) 512.

[2] H. Shichijo, R. Matyi, A. H. Taddiken and Y. -C. Kao: IEE Trans. Electron Devices **37** (1990) 548.

[3] R. Fischer, T. Henderson, J. Kim, W. T. Masselink, W. Kopp, H. Morkoç and C. W. Litton: Electron. Lett. **20** (1984) 945.

[4] R. Fischer, W. Kopp, J. Gedymin and H. Morkoç: Electron Devices **33** (1986) 1407.

[5] H. Choi, B. Tsaur, G. Metze, G. Turner and J. Fan: IEE Electron Device Lett. **6** (1984) 207.

[6] M. Askun, H. Morkoç, L. Lester, K. Duh, P. Smith, P. Chao, M. Longerbone and L. Erickson: Appl. Phys. Lett. **49** (1986) 1654.

[7] M. Yamaguchi and S. Kondo: Mat. Res. Soc. Symp. Proc. **145** (1989) 279.

[8] M. Yang, T. Soga, T. Jimbo and M. Umeno: Jpn. J. Appl. Phys. **33** (1994) 6605.

[9] T. Nonaka, M. Akiyama, Y. Kawarada and K. Kaminishi: Jpn. J. Appl. Phys. **23** (1984) L919.

[10] H. Shichijo, J. Lee, W. Mclevige and A. Taddiken: IEE Electron Device Lett. **8** (1987) 121.

[11] N. Wada, S. Sakai and M. Fukui: Jpn. J. Appl. Phys. **33** (1994) 1268.

[12] T. Egawa, H. Tada, Y. Kobayashi, T. Soga, T. Jimbo and M. Umeno: Appl. Phys. Lett. **57** (1990) 1179.

[13] H. K. Choi, C. A. Wang and N. H. Karam: Appl. Phys. Lett. **59** (1991) 2634.

[14] L. Pavesi and M. Guzzi: J. Appl. Phys. **75** (1994) 4779.

[15] M. Akiyama, Y. Kawarada and K. Kaminishi: Jpn. J. Appl. Phys. **23** (1984) L843.

[16] R. J. Matyi, H. Shichijo, T. M. Moore and H. -L. Tsai: Appl. Phys. Lett.**51** (1987) 18.

[17] J. P. van der Ziel, N. Chand and J. S. Weiner: J. Appl. Phys. **66** (1989) 1195.

[18] J. P. van der Ziel and N. Chand: J. Appl. Phys. **68** (1990) 2731.

[19] N. Wada, S. Sakai and M. Fukui: Jpn. J. Appl. Phys. **33** (1994) 976.

[20] Y. Ujiie and T. Nishinaga: Jpn. J. Appl. Phys. **28** (1989) 337.

[21] Y. H. Lo, R. Bhat, D. M. Hwang, C. Chua and C. -H. Lin: Phys. Lett.**62** (1993) 1038.

[22] S. Hasegawa, K. Maehashi, H. Nakashima, T. Ito and A. Hiraki: J. Cryst. Growth **95** (1989) 113.

[23] T. Yonehara, K. Sakaguchi and N. Sato: Appl. Phys. Lett. **64** (1994) 2108.

[24] N. Sato, K. Sakaguchi, K. Yamagata, Y. Fujiyama and T. Yonehara: J. Electrochem. Soc. **142** (1995) 3116.

[25] N. Sato, K. Sakaguchi, K. Yamagata, Y. Fujiyama, J. Nakayama and T. Yonehara: Jpn. J. Appl. Phys. **35** (1996) 973.

[26] T. Ueda, S. Nishi, Y. Kawarada, M. Akiyama and K. Kaminishi: Jpn. J. Appl. Phys. **25** (1986) 789.

[27] R. Fischer, D. Neuman, H. Zabel, H. Morkoç, C. Choi and N. Otsuka: Appl. Phys. Lett. **48** (1986) 1223.

[28] W. Stoltz, F. E. G. Guimaraes and K. Ploog: J. Appl. Phys. **63** (1988) 492

[29] G. Bernier, J. Beerens, J. DeBoeck, C. van Hoof and G. Borghs: Solid State Commun. **69** (1989) 729.

[30] T. Englert, G. Abstreiter and J. Pontcharra: Solid State Commun. **23** (1980) 31.

[31] D. E. Aspnes and A. A. Studna: Phys. Rev. B **27** (1983) 985.

[32] C. Nguyen, B. Brar, H. Kroemer and J. H. English: Appl. Phys. Lett. **60** (1992) 4613.

Chapter 6

Summary

The principle purpose of this study was to understand the fundamental properties mainly electrical and physical properties in GaN layer on sapphire substrate by theoretical calculation as well as experimental methods, and reduce the residual thermal stress in GaAs on Si substrate by introducing a new thin Si layer over porous Si substrate technology. In both materials, there can be no doubt that rich opportunities for material physical properties and device engineerings exist. The several properties of GaN were revealed and the symptom of overcoming the residual thermal stress by introducing a new Si substrate technology was revealed by this study. The results in this study are hopefully expected to give a helpful guidance for the realization of high-performance opto-electronic devices.

In chapter 1, the background and current status, the problems of the heteroepitaxial growth of GaN/sapphire and GaAs/Si and the purpose of this research were described.

Here the results obtained in this study are summarized as follows:

In chapter 2, the theoretical characteristics of high field and high temperature electron transport in both cubic and hexagonal phases of GaN as well as GaAs by Monte Carlo calculation and the temperature dependent hole transport in cubic phases of GaN by relaxation time approximation were discussed.

Overshoot effects were dominated in electron transport properties and the transit time in both phases GaN was comparable or less than that of GaAs in shorter distance. In comparison with hexagonal phase of GaN, the cubic phase of GaN has an advantage from the applied field electric dependent and temperature dependent velocity field. Furthermore, both phases concluded to be capable of same or higher frequency performance than GaAs. The calculation showed that the maximum operating frequency might be capable of achieving a f_T as high as 50 GHz in 1 μm GaN FETs.

The anisotropy factors, which determine hole mobilities, $r_{\mathrm{A1}} = 0.668$ and $r_{\mathrm{A2}} = 0.991$ were determined for the heavy and light hole bands, respectively using valence band parameters for the first time. It was demonstrated that the knowledge of the anisotropy parameter was essential for the evaluation of hole transport characteristics.

The calculations showed that the dominant lattice scattering mechanism for holes is the acoustic deformation potential. The results of calculations revealed the scattering by acoustic deformation potential plays an important role in determining the hole transport characteristics for the temperature between 50 and 300 K. As to ambiguity of the activation energies in the ionized impurities scattering mechanism, there was no significant difference on the scattering time in the ranges 100 - 250 meV at high compensation ratio (K=0.5 and 0.9). It was found that the hole transport characteristics were strongly affected on the compensation ratio.

In chapter 3, characteristics of A_1(LO)-phonon-plasmon coupled mode in various concentration of n- and p-type GaN on sapphire substrate and the residual thermal stresses in post-growth patterned n-type GaN on sapphire substrate characterized by Micro–Raman scattering technique at 300 K were discussed.

The carrier concentrations of n-type GaN, which were estimated by the line shape fitting of A_1(LO)-phonon-plasmon coupled mode, were compared with the results of Hall measurements and obtained good agreement. It was demonstrated that Raman measurement is suitable technique to determine the free-carrier concentration.

The p-type GaN did not show A_1(LO)-phonon-plasmon coupled mode clearly like a n-type case. The theoretical calculations revealed that both a characteristic of over-damped plasmon damping factor (plasmon damping factor $\gg$ plasmon frequency) and an effective hole mass affected this p-type phenomena. It was found that a clear continuum band in the low-frequency region below $\approx 350\ \mathrm{cm}^{-1}$ was observed in p-type GaN.

Reduction of the thermal stress in the post-growth patterned GaN on sapphire substrate was discussed. The relaxation of compressive stress was observed with decreasing the square size especially $\leq 40\ \mu$m. It was found that the internal stress is less important for the A_1(LO) phonon characteristic of GaN.

In chapter 4, the ESR properties of as-grown and electron irradiated hexagonal n-type GaN on sapphire substrate were presented. An single resonance at $g_{\parallel} = 1.9545$ and $g_{\perp} = 1.9451$ due to delocalized electrons in the conduction band or in a shallow impurity band was observed from as-grown n-type GaN.

The five-band $\mathbf{k}\cdot\mathbf{p}$ model using g value measured in this study, the matrix elements coupling between Γ_1 conduction and Γ_6 valence and its conduction bands, and spin-orbit splitting of the Γ_6 were estimated.

The observed ESR linewidth narrowing at low-temperature was concluded due to an averaging of nuclear hyperfine structures with lattice nuclei through motion of the electrons (hopping conduction) at $T \leq 25$ K and its broadening was concluded due to an electron-phonon interaction at $T \geq 25$ K.

The theoretical model based on rate equations was developed to explain the change of the luminescence ratio between the near-band-edge transition at 3.4 eV and the broad band emission centered around 2.2 eV with changing 7 MeV electron irradiation dose.

To overcome a low sensitivity of conventional ESR, the low-temperature light-induced ESR (LESR) was used to detect deep defect states, however, no deep defect state was revealed. The defect production rate was estimated and the energy necessary to create a Frenkel-pair (E_d) simultaneously from ESR or LESR analysis. The change of the intensity ratio was due to the Ga Frenkel-pair with energy necessary to create a Ga Frenkel $E_d = 30$ eV induced by 7 MeV electron irradiation. And the yellow luminescence was tentatively identified to be a radiative transition from a donor band to a V_{Ga} acceptor.

In chapter 5, the new thin Si layer on porous Si substrate was proposed to overcome the residual thermal stress in GaAs layer on Si substrate. A significant reduction of the residual tensile strain in the GaAs layer was confirmed by X-ray diffraction, low-temperature photoluminescence and Raman scattering measurements.

The disagreement of the stress values obtained by these methods was discussed in terms of characterization area of methods. The stress reduction mechanisms was also discussed. The obtained data clearly showed that this method is a promising substrate for overcoming the problems in GaAs/Si.

Compared to the selective-area growth or the post-growth patterning technique, this method is applicable to large areas of GaAs/Si.